

Infall, Outflow, Rotation, and Turbulent Motions of Dense Gas within NGC 1333 IRAS 4

James Di Francesco¹, Philip C. Myers, David J. Wilner,
Nagayoshi Ohashi², and Diego Mardones³
Harvard-Smithsonian Center for Astrophysics
60 Garden St., MS 42, Cambridge, MA 02138, U.S.A.

ABSTRACT

Millimeter wavelength observations are presented of NGC 1333 IRAS 4, a group of highly-embedded young stellar objects in Perseus, that reveal motions of infall, outflow, rotation, and turbulence in the dense gas around its two brightest continuum objects, 4A and 4B. These data have finest angular resolution of $\sim 2''$ (0.0034 pc) and finest velocity resolution of 0.13 km s^{-1} .

Infall motions are seen from inverse P-Cygni profiles observed in $\text{H}_2\text{CO } 3_{12}-2_{11}$ toward both objects, but also in $\text{CS } (3-2)$ and $\text{N}_2\text{H}^+ 1-0$ toward 4A, providing the least ambiguous evidence for such motions toward low-mass protostellar objects. Outflow motions are probed by bright line wings of $\text{H}_2\text{CO } 3_{12}-2_{11}$ and $\text{CS } (3-2)$ observed at positions offset from 4A and 4B, likely tracing dense cavity walls. Rotational motions of dense gas are traced by a systematic variation of the N_2H^+ line velocities, and such variations are found around 4A but not around 4B. Turbulent motions appear reduced with scale, given N_2H^+ line widths around both 4A and 4B that are narrower by factors of 2 or 3 than those seen from single-dish observations. Minimum observed line widths of $\sim 0.2 \text{ km s}^{-1}$ provide a new low, upper bound to the velocity dispersion of the parent core to IRAS 4, and demonstrate that turbulence within regions of clustered star formation can be reduced significantly.

A third continuum object in the region, 4B', shows no detectable line emission in any of the observed molecular species.

¹currently at the Radio Astronomy Laboratory, 601 Campbell Hall, University of California, Berkeley, Berkeley, CA, 94705-3411 U.S.A.

²currently at the Institute of Astronomy and Astrophysics, Academia Sinica, P.O. Box 1-87, Nankang, Taipei 11529, Taiwan, R.O.C.

³currently at the Departamento de Astronomía, Universidad de Chile, Casilla 36-D, Santiago, Chile

Subject headings: ISM: individual (NGC 1333 IRAS 4), ISM: kinematics and dynamics, stars: formation

1. Introduction

Star formation involves both coherent and incoherent gas motions within molecular clouds. Coherent motions are those with an implicitly common directionality, and include the infall, outflow, and rotational motions of molecular gas associated with extremely young protostellar objects (Mardones et al. 1997, henceforth M97); Gregersen et al. 1997; Bontemps et al. 1996; Ohashi et al. 1997). Incoherent motions have no directionality and appear random, and include thermal motions within molecular gas and nonthermal motions of turbulence (i.e., randomly propagating MHD waves; Arons & Max 1975).

Understanding gas motions is crucial to understanding the overall flow of mass during the star formation process, and this is typically attempted by analyzing molecular gas line profiles. In practice, however, different types of motion can be difficult to distinguish because similar line profiles can be produced when different molecular gas motions are projected along the line-of-sight. For example, asymmetrically-blue optically-thick lines relative to symmetric optically-thin lines have been interpreted recently as evidence for infall motions in several molecular cloud cores (e.g., see Leung & Brown 1977; Zhou et al. 1993). However, outflow or rotational motions of molecular gas can also produce such a signature, especially at velocities that are low relative to the systemic velocity (see Adelson & Leung 1988; Cabrit & Bertout 1986). In addition, thermal and nonthermal motions each act to broaden line widths, and together can potentially obscure signatures of other motions.

Analysis of the gas motions associated with star formation is further complicated by the fact that stars form in groups. For example, young stars are found by number more in close proximity within massive, turbulent cloud cores (as in Orion, Perseus, or Ophiuchus) than in isolation in less-massive, non-turbulent cores (as in Taurus or Lupus; see Lada, Strom, & Myers 1993). Given the finite resolutions of millimeter telescopes, the apparent proximity on the sky of several protostellar objects within a group can confuse the relationships between observed molecular gas motions and individual objects, especially in more distant regions.

Millimeter interferometers can minimize the problems of ascribing various types of motion to gas within regions where groups of young stellar objects are forming, by providing high-resolution observations of judiciously-chosen molecular lines. For example, lines observed at high resolution can yield profiles that are less ambiguous in interpretation. Furthermore, the high resolution can allow a better determination of the spatial association of gas with specific objects in a crowded field. In addition, high-resolution observations can reveal strikingly the abundance contrasts between outflowing and non-outflowing gas, so observing species particularly abundant in either of these components can better trace its

specific motions.

In this paper, we present millimeter interferometer observations of the NGC 1333 IRAS 4 region in the L1430 core of Perseus to probe the individual coherent and incoherent motions associated with a small group of protostellar objects. NGC 1333 itself is a region forming many protostellar groups, and has a 350 pc distance⁴ (Herbig & Jones 1983).

IRAS 4 consists of 4 (or more) very-embedded objects located within a 30'' (0.05 pc) radius, all $\sim 3'$ (0.3 pc) southeast of SVS 13. IRAS 4 was discovered by Jennings et al. (1987) as a single IRAS source, and later resolved by Sandell et al. (1991) into 4A and 4B, separated by 30''. Although 4A and 4B together were considered one of the first “protobinaries” ever detected (see Mathieu 1994), each object is itself multiple. IRAS 4A was resolved into 4A and 4A', with 2'' separation, by Lay, Carlstrom & Hills (1995), and IRAS 4B was resolved into two objects, 4B and 4B', with 10'' separation, by Looney, Mundy & Welch (2000). The 4B object itself also may be a binary or triple system of $< 0''.5$ separation, although this remains unconfirmed. The 4B' object has been named differently by other groups who detected it contemporaneously, i.e., 4BII by Smith et al. (2000), 4BE by Sandell & Knee (2000), and 4C by Looney et al. and Choi, Panis & Evans (1999). We name the object 10'' east of 4B as 4B' because 4C was used by Rodriguez, Anglada & Curiel (1999) and Sandell & Knee to name a millimeter object $\sim 40''$ east-by-northeast of 4A. The spectral energy distributions (SEDs) of 4A and 4B are both very red, suggesting that IRAS 4 consists of several “Class 0” objects, each at the earliest observed stage of protostellar evolution (i.e., $t \approx 10^4$ years or less; see André, Ward-Thompson & Barsony 1993).

IRAS 4 has been identified previously as a site of outflow and possibly infall in a turbulent region forming clusters. Using single-dish observations of numerous millimeter and submillimeter emission lines, Blake et al. (1995, henceforth B95) probed abundance depletions and enhancements in the gas associated with 4A or 4B. Low velocity line emission (i.e., at $\Delta V \approx 1\text{--}2$ km s⁻¹ relative to the systemic velocity) revealed a non-outflowing gas component around each source, with abundance depletions by factors of 10–20 (relative to dust) due to the adsorption of molecules onto grains at the high densities ($n = 2 \times 10^6$ cm⁻³) and low temperatures ($T_k = 20\text{--}40$ K) of the gas surrounding each object. The profiles of some optically-thick lines seen by B95 were asymmetrically-blue, suggesting these gas components were infalling. Outflowing gas around each source was also detected from line wings seen at higher relative velocities. Qualitative differences in the outflows were found between sources, e.g., the 4A outflow extended 4' tip-to-tip in CO and 1' tip-to-tip

⁴A distance to NGC 1333 of 220 pc has been suggested by Černis 1990, but we assume the 350 pc value for this paper.

in CS, but the 4B outflow extended only $<20''$ in either tracer. Despite these differences, however, abundance enhancements (relative to CO) were found in both outflows for several molecules including H_2CO , CS, and CH_3CO , likely due to the return of grain mantles to the gas phase from grain-grain collisions within outflow shear zones.

Further evidence for infall motions at 4A and 4B were obtained from the asymmetrically-blue profiles of H_2CO $2_{12}-1_{11}$ and CS $2-1$ by M97, and HCO^+ $4-3$ and HCO^+ $3-2$ by Gregersen et al. (1997). Mardones (1998, henceforth M98) further mapped IRAS 4 in H_2CO $2_{12}-1_{11}$ and H_2CO $3_{12}-2_{11}$ and found asymmetrically-blue profiles throughout the region, but the most extreme self-absorptions were found at the positions of 4A and 4B (see also Mardones et al. 2001). Choi, Panis & Evans mapped IRAS 4 in HCO^+ $1-0$ and HCN $1-0$, and again found asymmetrically-blue emission profiles at the positions of each protostellar object. In addition, small redshifted absorption dips were seen in their HCN spectrum toward 4A, arising from infalling gas along the line-of-sight.

We describe our millimeter interferometer observations in §2. A description of the H_2CO $3_{12}-2_{11}$, CS $3-2$, and N_2H^+ $1-0$ data is presented in §3. Discussion of the infall and outflow motions revealed by H_2CO and the rotational and turbulent motions revealed by N_2H^+ follows in §4. In §5, a concluding summary is presented. An Appendix describes the continuum data and the relative millimeter SEDs of 4A, 4B, and 4B'.

2. Observations

IRAS 4 was observed between July 1997 and March 1998 at the IRAM⁵ Plateau de Bure Interferometer (PdBI), NRO⁶ Nobeyama Millimeter Array (NMA), and the NRAO⁷ Very Large Array (VLA). Table 1 lists the wavelengths, frequencies, configurations, and dates of observations made with each array, as well as the synthesized beam FWHMs and the 1σ (rms) continuum sensitivities obtained from combining all respective tracks.

⁵The Institut de RadioAstronomie Millimétrique (IRAM) is an international institute for research in millimeter astronomy, and is supported by the CNRS (Centre National de la Recherche Scientifique, France), the MPG (Max Planck Gesellschaft, Germany), and the IGN (Instituto Geografico Nacional, Spain).

⁶The Nobeyama Radio Observatory (NRO) is a branch of the National Astronomical Observatory, an interuniversity research institute operated by the Ministry of Education, Science, and Culture, Japan.

⁷The National Radio Astronomy Observatory (NRAO) is a facility of the National Science Foundation, U.S.A., operated under cooperative agreement by Associated Universities, Inc.

2.1. Primary Observations

2.1.1. PdBI Data

At the IRAM PdBI, H₂CO 3₁₂–2₁₁ at 225.7 GHz was observed to trace infall or outflow motions in the region, following M97 or B95 but using other H₂CO transitions and at higher resolution. Dense gas can be traced by this line, as its critical density $n_{cr} \approx 7 \times 10^6 \text{ cm}^{-3}$ (from Green 1991), but H₂CO may be depleted in dense gas surrounding protostellar objects and enhanced in outflows (see B95). In addition, N₂H⁺ 1–0 at 93.17 GHz was observed to trace non-outflowing dense gas in IRAS 4, following M97 but at higher resolution. This line is abundant in star-forming regions (e.g., Womack, Ziurys & Wyckoff 1992) and has also a high critical density, i.e., $n_{cr} \approx 2 \times 10^5 \text{ cm}^{-3}$. Furthermore, N₂H⁺ is observed and predicted to remain relatively abundant in dense cores with $n \approx 10^{4-5} \text{ cm}^{-3}$ (Benson, Caselli, & Myers 1998, Bergin & Langer 1997), but is possibly depleted, rather than enhanced, by outflow chemistry (see Bergin, Neufeld & Melnick 1998). Continuum emission at $\lambda = 3.2 \text{ mm}$ and $\lambda = 1.3 \text{ mm}$ was observed to locate each protostellar object in IRAS 4 from associated warm dust.

The 1 mm and 3 mm bands were observed simultaneously. Receiver 2 was tuned to observe H₂CO 3₁₂–2₁₁ over 230 channels in a 20 MHz wide band, yielding a channel spacing of 0.10 km s^{–1} or a velocity resolution of 0.13 km s^{–1}. The remaining 2 correlator units were assigned to observe continuum emission at $\lambda = 1.3 \text{ mm}$ over a 300 MHz wide band. Receiver 1 was tuned to observe N₂H⁺ 1–0 over 230 channels in a 10 MHz wide band, allowing all 7 of its hyperfine components to be sampled with a channel spacing of 0.13 km s^{–1}, or a velocity resolution of 0.16 km s^{–1}. The other 2 correlator units were combined to observe continuum emission at $\lambda = 3.2 \text{ mm}$ in a 300 MHz wide band.

Each track with the IRAM PdBI consisted of 3 pointings centered on 4A, 4B, and a position halfway in-between, interleaved with observations of 0415+379 (3C 111) or 0316+413 (3C 84) for phase and flux calibration. (The sources 2230+114 and MWC 349 were also observed as secondary flux calibrators.) With primary beam FWHMs of $\sim 54''$ and $\sim 22''$ at 93.17 GHz and 225.7 GHz respectively, this pointing strategy allowed the construction of an over-sampled mosaic at $\lambda = 3.2 \text{ mm}$ and an under-sampled mosaic at $\lambda = 1.3 \text{ mm}$. Each track was calibrated in Grenoble, France using the IRAM software package CLIC. Data from each pointing were combined in the visibility plane and inverted simultaneously, and the resulting mosaics cleaned using the IRAM software package MAPPING. Further analysis was carried out using the MIRIAD, CLASS, and AIPS software packages.

2.2. Secondary Observations

2.2.1. NRO NMA Data

The CS 3–2 line at 146.97 GHz was observed at the NRO NMA in order to trace dense gas, as its $n_{cr} \approx 1.3 \times 10^6 \text{ cm}^{-3}$ (Evans 1999). Continuum emission at $\lambda = 2.2 \text{ mm}$ and $\lambda = 2.0 \text{ mm}$ was observed in order to trace warm dust, improving the SED of each source.

The NMA FX correlator was tuned to observe CS 3–2 at 146.97 GHz, over 1024 channels in a 32 MHz wide band, for a channel spacing and velocity resolution of 0.064 km s^{-1} . The NMA Ultra-Wide Bandwidth Correlator was tuned over a 1024 MHz wide band to observe simultaneously continuum emission at $\lambda = 2.2 \text{ mm}$ and $\lambda = 2.0 \text{ mm}$ in the lower and upper sidebands respectively.

Each track with the NRO NMA consisted of 2 pointings centered on 4A and 4B, interleaved with observations of 0316+413 (3C 84) for phase and flux calibration. With a primary beam at 146.97 GHz of $\sim 51''$, this pointing strategy resulted in slightly under-sampled mosaics at $\lambda = 2.2 \text{ mm}$ and $\lambda = 2.0 \text{ mm}$. Data from each track were calibrated in Nobeyama, Japan, using the software package UVPROC2. Further analysis was carried out using the MIRIAD software packages. For better sensitivity of CS 3–2, the NMA data were tapered with a $4'' \times 4''$ FWHM Gaussian to obtain a final $6''.5 \times 4''.4$ FWHM synthesized beam.

2.2.2. NRAO VLA Data

Continuum emission at $\lambda = 6.9 \text{ mm}$ and $\lambda = 1.3 \text{ cm}$ was observed with the NRAO VLA to trace dust, extending the SED of each source across the entire millimeter wavelength range. Observations at these wavelengths are also important because they set effective limits on the amounts of free-free emission within the SEDs of young stellar objects at shorter millimeter wavelengths, allowing the amounts of thermal emission solely from dust to be characterized more accurately (e.g., see Di Francesco et al. 1997).

Both bands were observed simultaneously by dividing the VLA into two sub-arrays, with 13 antennas observing at $\lambda = 6.9 \text{ mm}$ (43.34 GHz) using Q-band receivers, and 14 antennas observing at $\lambda = 1.3 \text{ cm}$ (22.46 GHz) using K-band receivers, each over 100 MHz wide bands.

The NRAO VLA was pointed at 1 position halfway between 4A and 4B to include 4A, 4B, and 4B' within the $\sim 62''$ and $\sim 120''$ primary beam FWHMs of the VLA antennas at

$\lambda = 6.9$ mm and $\lambda = 1.3$ cm respectively. Observations of IRAS 4 were interleaved with observations of 0316+413 (3C 84) for phase calibration approximately every 10 minutes and X-band reference pointing checks approximately every 60 minutes. Observations of 0134+329 (3C 48) and 1328+307 (3C 286) were made for flux calibration at both wavelengths. Data from this track were calibrated in Socorro, U.S.A., and further analyzed using the software package AIPS.

3. Results

Figure 1 shows maps of IRAS 4 in continuum emission at $\lambda = 1.3$ mm, $\lambda = 2.0$ mm, and $\lambda = 3.2$ mm, as well as maps of the integrated intensities of the H_2CO $3_{12}-2_{11}$, CS $3-2$, and N_2H^+ $1-0$ line emission (i.e., the “zeroth-moment” obtained at a given position by summing emission from all channels except those containing values $< 2 \sigma$.)

3.1. Continuum

Figures 1a, 1b, and 1c illustrate the relative positions (in projection) of protostellar continuum objects in IRAS 4, namely 4A, 4B, and 4B' at 3 different wavelengths. These objects were also detected at $>4 \sigma$ at $\lambda = 2.2$ mm and $\lambda = 6.9$ mm, but only 4A and 4B were detected at $\lambda = 1.3$ cm. Table 2 lists flux densities measured from our data (also see Appendix.)

Separated from 4A by only $\sim 1''$, 4A' is not detected distinctly from 4A in our $\sim 2-4''$ resolution maps, but the continuum emission around 4A is extended towards its position. For this paper, we limit discussion of 4A and 4A' as an unresolved pair rather than consider them individually, i.e., $4A = (4A + 4A')$. Similarly, we refer to the 4B object as 4B, though it may also be multiple. Furthermore, the nearby source 4C was not observed as it lay outside the fields-of-view of our PdBI and NMA mosaics, and our VLA images did not have sufficient sensitivity to detect it (based on its flux densities at $\lambda = 3.6$ cm and $\lambda = 6.0$ cm; see Rodriguez et al.)

3.2. H_2CO $3_{12}-2_{11}$ and CS $3-2$

Figures 1d and 1e show that H_2CO and CS are distributed similarly around 4A, 4B, or 4B', but remarkable differences are found between objects. Near 4A, an extended lobe is located to the south-to-southeast and 1 or 2 compact spots are located to the north in both

H₂CO and CS. The southern lobe contains 4 local maxima in the H₂CO data, but only 2–3 maxima in the lower-resolution CS data. Near 4B, 2 single-peaked, compact lobes are seen to the north and south, with similar brightnesses in H₂CO but very different brightnesses in CS. In addition, three less prominent peaks to the east, northwest and southeast of 4B are detected in H₂CO but not in CS. Finally, no H₂CO or CS emission is detected near 4B'. In our H₂CO map, this source is located at the mosaic edge, making it unclear if the lack of detected H₂CO near 4B' is real or due to reduced sensitivity. In our CS map, however, 4B' is positioned well within the fields-of-view, but no CS is detected near the object.

Figure 2 shows grids of H₂CO 3₁₂–2₁₁ spectra from positions centered on 4A and 4B, spaced regularly in 2'' increments of R.A. or Dec., i.e., ~ 1 FWHM of the synthesized beam. The velocity range of each panel is centered at +6.96 km s⁻¹, the average central velocity determined from N₂H⁺ 1–0 data of 4A and 4B (see §4.3.2 below), which we consider here to be the systemic velocity of the IRAS 4 group.

Figure 2a reveals that at the 4A position (i.e., the central grid panel), an “inverse P-Cygni” line profile of blue-shifted emission and red-shifted absorption is clearly detected. The absorption feature has a central velocity of 7.6 km s⁻¹ and a width of ~ 0.9 km s⁻¹, and is not prominent at any other grid location. The maximum depth of the absorption toward 4A is ~ 9 K, or 1.3 Jy beam⁻¹, approximately equal to the peak intensity of $\lambda = 1.3$ mm continuum emission detected at the same position (see Table 2). With single-dish data, M98 detected asymmetrically-blue, single-peaked H₂CO emission with no absorption at the 4A position. North of 4A, the H₂CO spectra are double-peaked, with a dip at ~ 7.7 km s⁻¹, and a weak red wing is seen. South of 4A, the H₂CO spectra are single-peaked, but a strong blue wing is seen. The emission spot due north of 4A in Figure 1d almost entirely consists of this red-shifted wing emission. (The apparent H₂CO emission spot northwest of 4A is incidental map-edge noise.) The extended lobe seen south-to-southeast of 4A in Figure 1d almost entirely consists of blue-shifted wing emission.

Figure 2b reveals an inverse P-Cygni line profile at the 4B position (at the center of this grid, defined similarly to Fig. 2a). Here, the absorption has a central velocity of 7.9 km s⁻¹ and a width of ~ 1.0 km s⁻¹. The maximum depth of the absorption feature toward 4B is ~ 4 K, or 0.57 Jy beam⁻¹, again approximately equal to the peak intensity of continuum emission at $\lambda = 1.3$ mm. In addition, absorption is not prominent at positions offset from the continuum object. M98 also only detected asymmetrically-blue, single-peaked H₂CO emission with no absorption below the continuum at the 4B position. Furthermore, spectra to the north of 4B are double-peaked and a red wing is seen, like that seen north of 4A and also with a self-absorption at ~ 7.7 km s⁻¹. South of 4B, the line is single-peaked and a blue wing is found, similar to the line south of 4A. The bright peaks north or south of 4B seen

in Figure 1d predominantly consist of either red- or blue-shifted wing emission respectively, and the secondary features seen northwest and southeast of 4B consist of blue-shifted and red-shifted emission respectively. (The third emission feature seen in Figure 1d near 4B is off the eastern edge of the grid in Figure 2b, and has both blue- and red-shifted emission.)

Line profiles similar to those found for $\text{H}_2\text{CO } 3_{12}-2_{11}$ in Figure 2 are also seen for the CS 3–2 line at similar positions, including an absorption feature at 7.8–8.0 km s^{-1} in the CS spectrum at 4A, and a possible analogue at 4B. These data are not shown since they corroborate the H_2CO data, but are noisier and have lower spatial resolution.

3.3. $\text{N}_2\text{H}^+ 1-0$

Figure 1f shows the integrated intensity (zeroth-moment) of $\text{N}_2\text{H}^+ 1-0$ emission around the IRAS 4 objects. These distributions differ significantly from those of H_2CO and CS (Figures 1d and 1e) around each object. However, the spatial distribution of the integrated intensity also differs from object to object. Near 4A, the N_2H^+ emission is elongated northeast-southwest, extending somewhat symmetrically 10–15'' around a bisecting channel at position angle (P.A.) $\approx 45^\circ$ containing 4A and 4A'. Near 4B, the N_2H^+ emission is more compact than that near 4A, although it is slightly elongated north-south. In addition, N_2H^+ emission is coincident with the 4B object, unlike at 4A (i.e., no bisecting channel is seen in the zeroth-moment map.) Near 4B', N_2H^+ is not detected, although its position here is well within the field-of-view, unlike in the H_2CO mosaic.

Figure 3 shows grids of spectra of $\text{N}_2\text{H}^+ 101-012$, at the same positions at and around 4A and 4B shown in Figure 2. (For clarity, only the “isolated” hyperfine component of $\text{N}_2\text{H}^+ 1-0$ is shown.) Since the 2'' spacing of panels in Figure 3 corresponds approximately to half-beam spacing at the FWHM of the synthesized beam at 93.2 GHz, neighboring panels are not independent, as in Figure 2. (In addition, the velocity range of these grid panels differs from that of Figure 2, but remains centered at the same systemic velocity.)

Figure 3a reveals (in the central panel) another inverse P-Cygni line profile at the 4A position, with absorption of central velocity and width similar to those of H_2CO at the same position, i.e., 7.9 km s^{-1} and $\sim 1 \text{ km s}^{-1}$ respectively. (Absorption seen here in adjacent panels is still coincident with the continuum object due to the half-beam, non-independent grid spacing.) Unlike the H_2CO absorption, the peak depth is only $\sim 1.2 \text{ K}$, or $\sim 50\%$ the peak continuum intensity of 4A at $\lambda = 3.2 \text{ mm}$. M98 did not detect absorption of $\text{N}_2\text{H}^+ 1-0$ in their single-dish data at the 4A position. At positions northwest and southeast of 4A, the line is single-peaked in emission only with small shifts in central velocity to the red

and blue respectively. No systematic line width variations or wing emission is seen. The bisecting channel at a P.A. $\approx 45^\circ$ seen in Figure 1f is noticeable here from the relatively dim emission found in panels on the northeast-southwest diagonal.

Figure 3b shows that an inverse P-Cygni line profile is *not* seen at the position of the 4B object, rather a fairly symmetric line is found peaking at 7.1 km s^{-1} , near the systemic velocity. (Absorption may be present at $\sim 8 \text{ km s}^{-1}$ in the grid panel $2''$ west of the central position, but this is not suggested in any other adjacent, non-independent grid panel.) Unlike near 4A, there does not appear to be substantial variations in central velocity over the grid, but the line is dimmer and broader south of 4B and brighter and narrower north of 4B. Like near 4A, there is no evidence for wing emission. M98 detected a similarly-shaped single-peaked line profile at the 4B position.

4. Discussion

4.1. Distinct Tracers of Specific Motions

The spectral and spatial distributions of the lines described in §3 trace quite distinctly specific types of motion within IRAS 4. Infall is traced from the inverse P-Cygni profiles detected in H_2CO toward both 4A and 4B (and also in CS and N_2H^+ toward 4A alone.) Outflows from 4A and 4B are traced distinctly from infall, at positions offset from the protostellar objects, from H_2CO and CS lines with profiles of only bright line wings and no line cores. Rotation of non-outflowing dense gas around 4A or 4B is traced distinctly from outflow from spatial variations of the central velocity of N_2H^+ , with profiles of only line cores and no line wings. Furthermore, variations of turbulent motions within the non-outflowing dense gas about 4A and 4B are traced by spatial variations of the line width of N_2H^+ in the same profiles.

The observed lines distinctly trace specific motions partly because of the differing gas-grain chemistry of the molecular species. B95 suggested H_2CO and CS were depleted in the non-outflowing gas associated with 4A and 4B, due to significant amounts of these molecules adsorbing onto dust grains. Detailed models by Bergin & Langer (1997) of relative abundances in centrally-condensed cores of increasing density support this scenario, showing H_2CO or CS may deplete by ≥ 2 orders of magnitude at densities of $n \approx 10^5 \text{ cm}^{-3}$ onto grains with H_2O or CO mantles. These models, in turn, also suggest that N_2H^+ remains at a constant abundance to densities of $\sim 10^6 \text{ cm}^{-3}$, due to the low binding energy of N_2 , its precursor molecule, to grain mantles. Therefore, we expect that N_2H^+ traces non-outflowing dense gas better than H_2CO or CS in a suitably dense protostellar core.

In contrast, B95 suggested the enhanced abundances of H_2CO and CS found in the line wings were due to significant amounts of these molecules returning to the gas phase from the disruption of grain mantles in the outflows. Moreover, the single-dish data of M97 show the N_2H^+ 1–0 components at 4A and 4B have Gaussian profiles, with no emission at the wing velocities of H_2CO or CS . Models of molecular abundance variations from post-shock chemistry by Bergin et al. support this contrast, since the increased abundance in outflows of H_2O , returned to the gas phase from grain mantles, appears to rapidly deplete N_2H^+ . Therefore, we expect H_2CO or CS traces better outflowing gas than N_2H^+ . Such molecular abundance contrasts are not unique to IRAS 4 and have been observed similarly elsewhere, e.g., the single-dish observations of the L1157 core and outflow by Bachiller & Pérez-Gutiérrez (1997).

Another important reason our data distinctly trace specific motions is their high spatial resolution. For example, interferometers allow detection of the inverse P-Cygni profiles because the brightnesses of the continuum objects in the relatively small beams can exceed the brightnesses of line emission from intervening, infalling gas along the line-of-sight, leading to red-shifted absorption. (Blue-shifted emission in the inverse P-Cygni profiles arises from concentrated gas on the far sides of the protostellar objects.) In addition, the spatial filtering properties of the interferometer can further distinguish specific motions better than single-dish observations, especially at low relative velocities, by selectively sampling the kinematics of compact structures, and resolving out confusing, extended emission. For example, outflowing gas is detected more distinctly in interferometer observations of H_2CO or CS , beyond abundance differences, because zones of outflowing dense gas are expected to be more compact, and hence are more easily seen by an interferometer, than the outer, less-dense layers of a circumstellar envelope that may still contain abundant H_2CO or CS . On the other hand, interferometers can still detect non-outflowing gas in such an envelope using N_2H^+ because, unlike H_2CO or CS , it remains relatively abundant in the denser and more-compact inner regions that are less resolved out than outer regions. (As described below, N_2H^+ may be somewhat depleted relative to “canonical” values in IRAS 4.)

4.2. H_2CO Observations

4.2.1. *Infall*

Detections of red-shifted absorption indicative of infall motions have been made primarily toward high-mass young stellar objects, where the absorption profiles were seen against the continuum emission of bright HII regions in interferometer beams. For example,

red-shifted absorption was seen toward G10.6–0.4 in NH_3 (1,1) and (3,3) by Keto, Ho & Haschick (1987, 1988; with VLA beams of $3''.0$ FWHM and $0''.3$ FWHM respectively). Similar profiles were also detected toward W51:e2 in NH_3 (1,1) and (2,2) by Ho & Young (1996; with VLA beams of $2''.6$ – $3''.8$ FWHM), and in these transitions plus NH_3 (3,3) by Zhang & Ho (1997; with VLA beams of $0''.2$ – $1''.0$ FWHM), and in CS 3–2 by Zhang, Ho & Ohashi (1998; with an NMA $1''.1$ FWHM beam). Furthermore, an inverse P-Cygni profile was noted toward W49A North:G in HCO^+ 1–0 by Welch et al. (1987; with a BIMA $\sim 7''$ FWHM beam).

Toward low-mass young stellar objects, detections of red-shifted absorption against continuum emission have been very rare, the only case being the weak inverse P-Cygni profile detected in the HCN 1–0 line toward NGC 1333 IRAS 4A by Choi, Panis & Evans with a BIMA ~ 8 – $12''$ FWHM beam. (Red-shifted absorption is also suggested in their Figure 1f in the HCN line toward IRAS 4B, and in the HCO^+ 1–0 line toward both objects, but they describe only the HCN line toward 4A as an inverse P-Cygni profile.)⁸

Figure 4 shows the H_2CO 3_{12} – 2_{11} line at positions of maximum continuum intensity from 4A and 4B (enlarged from the central panels of Figures 2a and 3a.) These data provide the least ambiguous evidence for infall motions toward low-mass young stellar objects. First, the detection of the absorption here is very strong, given the low channel-to-channel noise of these data. Second, the excitation requirements of the lower energy level of the H_2CO 3_{12} – 2_{11} transition (i.e., $E_{2_{11}}/k = 7.5$ K) are higher than those of HCN 1–0, suggesting the absorptions are more likely occurring in warmer gas associated with the young objects, rather than in a layer of cooler gas at slightly higher velocity situated along the line-of-sight (and possibly not associated with the young objects.) In addition, the scales probed by these data are smaller than other investigations. At a distance of 350 pc, the linear beam size (FWHM) of the H_2CO data at IRAS 4 is ~ 0.003 pc, a factor of ~ 4 – 6 less than the scales probed by Choi et al., and a factor of ~ 2 less than those probed with inverse P-Cygni profiles at the more-distant, higher-mass objects noted above.

To probe conditions in the absorbing gas, the inverse P-Cygni profiles toward 4A and 4B were modeled with an enhanced version of the “two-layer” code used by Myers et al. (1996) to reproduce successfully the appearance of spectral lines from infalling gas toward several protostellar cores (see also Williams & Myers 2000, and Lee, Myers & Tafalla 2001) In this version, two layers, located along the line-of-sight, each have peak optical depth τ_o , velocity dispersion σ , and approach speed V_{in} toward a continuum source

⁸An inverse P-Cygni profile of the ^{13}CO (2–1) line toward 4A has been also recently detected by Webster & Welch (2000) with a BIMA $6''.7$ FWHM beam.

located in-between. The continuum source is assumed to be optically thick with a Planck temperature J_c , where J_c is related to the blackbody temperature T_c at frequency ν by $J_c = T_o/(\exp(T_o/T_c)-1)$, with $T_o = h\nu/k$, $h =$ Planck’s constant, and $k =$ Boltzmann’s constant. The continuum source also fills a fraction Φ of the telescope beam area. The “front” layer between source and observer has a Planck excitation temperature J_f while the “rear” layer behind the source has a Planck excitation temperature J_r . The rear layer is illuminated by the cosmic background radiation of Planck temperature J_b .

For this system, the observed line brightness temperature at velocity V can be written as

$$\Delta T_B = (J_f - J_{cr})(1 - \exp(-\tau_f)) + (1 - \Phi)(J_r - J_b)(1 - \exp(-\tau_r - \tau_f)), \quad (1)$$

where

$$J_{cr} = \Phi J_c + (1 - \Phi)J_r, \quad (2)$$

and,

$$\tau_f = \tau_o \exp(-(V - V_{in} - V_{LSR})^2/2\sigma^2), \quad (3a)$$

$$\tau_r = \tau_o \exp(-(V + V_{in} - V_{LSR})^2/2\sigma^2). \quad (3b)$$

In this model, the line profile can be understood very simply from Equation 1 as the linear sum of a broad positive profile centered on V_{LSR} (i.e., the right term of RHS) and a narrow negative profile centered on $V_{LSR}+V_{in}$ (i.e., the left term of RHS). If the systematic motion of the layers is inward (i.e., $V_{in} > 0$), Equation 1 implies that the resulting profile shows red absorption or “infall asymmetry.” If the front layer is cooler than the continuum source and rear layer by a relatively small temperature differences $J_f - J_{cr}$, the asymmetric profile shows “self-absorption” but remains positive at all velocities. As this temperature difference increases, the profile becomes more asymmetric and its “dip” goes below the spectral baseline.

Equations 1-3 are essentially the same as Equations 1 and 2 of Myers et al. (1996), except that the emission from an optically thick central source is now included. This model is intended to give the simplest possible description of a contracting or expanding system which can reproduce the observed line profiles. Therefore, it gives only the crudest

picture of the optical depth and excitation temperature of the absorbing and emitting gas. However, the model is still useful for comparing the characteristic velocity V_{in} from one line profile to the next, since the ratio V_{in}/σ is most important to setting the line profile for any model of a contracting system (Leung & Brown 1977).

In addition to the observed spectra, Figure 4 shows model inverse P-Cygni profiles that successfully reproduce those observed. The respective model parameters are listed in Table 3. Infall speeds of $V_{in} = 0.68 \text{ km s}^{-1}$ and 0.47 km s^{-1} are obtained toward 4A and 4B respectively. (The blue wing in the 4A spectrum is likely from outflow and so it is not fit by the model.) Using essentially the same two-layer model (but without a continuum object), M98 found a V_{in} of only 0.11 km s^{-1} for the IRAS 4 region from the same H_2CO line. The difference between these results is likely because the spectrum modeled by M98 was obtained with a resolution coarser by a factor of ~ 6 than those shown here, and consisted of data averaged over the FWHM of their single-dish integrated intensity map, i.e., over a projected distance from the source of $\sim 0.04 \text{ pc}$. The resulting emission spectrum included data from positions offset from 4A and 4B with gas having possibly lower apparent infall velocities due to projection, whereas the inverse P-Cygni profile traces material along the line-of-sight to 4A or 4B with minimal projection effects.

The inverse P-Cygni profiles alone cannot demonstrate whether the infalling material consists of dense gas individually surrounding 4A or 4B, or from a common layer surrounding both objects, since infalling material at projected locations between 4A and 4B is not traced. However, the difference between V_{in} toward 4A and 4B is significant in that the range of V_{in} able to reproduce well each spectrum is only a few hundredths of km s^{-1} , if all other parameters are kept fixed. Different values of V_{in} toward 4A and 4B suggest the absorptions arise in dense gas residing around each source rather than in a layer common to both objects, where presumably more similar velocities toward 4A and 4B would be found.

From simple gravitational arguments, the line-of-sight speeds implied by the absorptions allow crude estimates of the masses of the 4A and 4B objects, assuming the infall speeds V_{in} arise from the velocity gain of gas free-falling from rest at $r = \infty$ to $r = r_{in}$, or

$$M = (V_{in}^2 r_{in})/2G = 1.2 \left(\frac{V_{in}}{1.0 \text{ km s}^{-1}} \right)^2 \left(\frac{r_{in}}{0.01 \text{ pc}} \right) M_{\odot}. \quad (4)$$

To obtain (an upper limit of) r_{in} , the mass obtained from Equation 4 can be equated with that within a sphere of radius r_{in} of mean density n , i.e., $M = (4/3)\pi r_{in}^3 n \mu m_H$, with μ equal to the mean molecular weight (2.32), and m_H equal to the mass of hydrogen. We assume $n = 2.3 \times 10^6 \text{ cm}^{-3}$, the critical density of the H_2CO $2_{11}-1_{10}$ line, a sufficient density for

substantial population of the 2_{11} energy level of H_2CO , determined at $T_k = 30$ K (Green 1991) since B95 estimated a kinetic temperature of non-outflowing gas around 4A of 20–40 K. Accordingly, the values of V_{in} obtained for 4A and 4B yield values of r_{in} of 0.0099 pc and 0.0068 pc respectively, or $5.8''$ and $4.0''$ respectively at the assumed distance of IRAS 4. These radii are smaller by factors of 1.4–2.2 than those obtained using integrated N_2H^+ 1–0 emission (see Figure 1f) to trace the projected extents of dense gas around 4A and 4B, which is consistent given the lower critical density of that transition.⁹ Using Equation 4, the masses interior to the respective values of r_{in} are $0.53 M_\odot$ and $0.17 M_\odot$ for 4A and 4B, reasonable values given the moderate luminosities of these objects and their location within a region of low-mass star formation.

Mass accretion rates, \dot{M}_{in} , can be estimated toward 4A and 4B using the simple expression: $\dot{M}_{in} = 4\pi r_{in}^2 \mu m_H n V_{in}$, or

$$\dot{M}_{in} = 1.7 \times 10^{-4} \left(\frac{r_{in}}{0.01 \text{ pc}} \right)^2 \left(\frac{n}{2.3 \times 10^6 \text{ cm}^{-3}} \right) \left(\frac{V_{in}}{1.0 \text{ km s}^{-1}} \right) M_\odot \text{ yr}^{-1}, \quad (5)$$

assuming spherical symmetry of the infall. With the values of V_{in} , n , and r_{in} described above, we estimate $\dot{M}_{in} = 1.1 \times 10^{-4} M_\odot \text{ yr}^{-1}$ for 4A, and $3.7 \times 10^{-5} M_\odot \text{ yr}^{-1}$ for 4B, using Equation 5. Assuming these rates are constant, accretion timescales t_{acc} can be then estimated by dividing the masses found above with the accretion rates. Such a calculation yields $t_{acc} = 4.7 \times 10^3 \text{ yr}$ and $4.6 \times 10^3 \text{ yr}$ for 4A and 4B respectively, remarkably similar and well within the $t_{acc} < 10^4$ surmised for Class 0 objects.

If the isothermal sound speed of this gas can be approximated as $V_{rms} = (kT_k/\mu m_H)^{1/2}$ and $T_k \approx 30$ K, the values obtained here for V_{in} suggest the infall motions toward 4A or 4B are supersonic, by factors of 2.1 and 1.4 respectively. Given that the magnetic field strength is poorly known in IRAS 4, however, it is not clear if the infall motions are also sub- or super-Alfvénic. From a virial theorem argument, Akeson et al. (1996) estimated large magnetic field strengths associated with 4A of 5–8 mG, suggesting the infall flows are very sub-Alfvénic. However, the summary of actual magnetic field measurements (of other various molecular clouds) by Crutcher (1999) suggests these values may be too large by factors of ~ 10 –100. If the infall motions are occurring exactly at the Alfvén speed (i.e., $V_A = B/(4\pi\mu n m_H)^{1/2}$ with $n = 2.3 \times 10^6 \text{ cm}^{-3}$, the required magnetic field strengths near 4A and 4B would be $720 \mu\text{G}$ and $500 \mu\text{G}$ respectively.

⁹Non-outflowing H_2CO in emission, i.e., over the velocities traced by N_2H^+ , is difficult to see around 4A and 4B, possibly due to low abundances or the relative brightness of the outflows.

The two-layer models used to compute the line profiles seen in Figure 4 neglect the radial variations in density, temperature, and velocity expected within protostellar envelopes. Therefore, these results are too simple to be definitive, but provide motivation for more observations and models of inward motions. It will be useful to make more-detailed, Monte-Carlo models of radiative transfer through envelopes, of the H_2CO line from these and other Class 0 objects.

4.2.2. Outflow

4.2.2.1 Outflow Morphologies and Origins

Figure 5 shows channel maps of H_2CO $3_{12}-2_{11}$ emission near 4A, revealing the underlying structure of the blue 4A outflow lobe better than the integrated intensity map (Figure 1d). In channel maps, the blue lobe consists of two prominent features south-by-southwest and southeast of 4A. Increasing in relative velocity, emission from the first feature is first seen at 6.5 km s^{-1} , and it peaks at increasing angular separations from 4A in a Hubble Law manner reminiscent of other protostellar outflows (see Bachiller 1996). At 2.0 km s^{-1} , however, the angular separations of the peaks of this feature shift to the southeast with increasing velocity out to the band edge, -10 km s^{-1} . The second feature is first seen at 6.8 km s^{-1} and it moves south and west with increasing relative velocity in a manner less consistent with a Hubble Law. Together, these features resemble cavity walls of an outflow seen at increasing relative velocities. In contrast to Figure 1d, the channel maps suggest the 4A blue lobe has an overall P.A. of $\sim 160^\circ$, and its north-south appearance in Figure 1d is due to the relative brightness of the western cavity wall. Figure 5 also shows dense gas outflowing from 4A', the binary companion to 4A, at low relative velocities along the south-by-southwest feature, but dense gas appears to be outflowing instead from 4A at higher relative velocities.

Our H_2CO data reveal a systematic decrease in the P.A. of the 4A outflow axis with scale that could be due to precession of the 4A outflow axis (i.e., a systematic change in its P.A. with time.) Single-dish CS data from B95 and Lefloch et al. (1998) show the blue lobe oriented southwest at separations $>35''$ from 4A but oriented south at separations $15-35''$ from 4A. Our data show this trend continues to smaller separations, since the blue lobe is oriented to the southeast at $<15''$ offsets from 4A. Such precession may be due to the binarity of 4A, if the gravitational action of 4A' on 4A is strong enough (or vice-versa.) The inherent periodicity of precession, however, suggests outflow gas will be distributed periodically in P.A. at even larger scales, and indeed such evidence may exist in recent CO maps of NGC 1333. For example, a CO $3-2$ JCMT map of Knee & Sandell (2000) shows

what may be the northern red lobe of the 4A outflow curving north of IRAS 4, from a P.A. of 45° to a P.A. of 0° over 3–4'. In addition, the CO 1–0 BIMA mosaic of NGC 1333 by Plambeck & Engargiola (1999) faintly shows possible emission from the 4A outflow at large scales, curving symmetrically over several arcminutes from 4A in an S-shape. However, maps that are more sensitive than these are required to determine conclusively if this distant emission is actually related to the 4A outflow. (As this paper was being revised after submission, a periodicity in the P.A. of the 4A outflow was seen by Choi (2001). However, the amplitude suggested here is larger by a factor of ~ 10 .)

The difference in integrated intensity between sides of the 4A blue lobe could be understood if the outflow is precessing, as dense gas surrounding 4A may be cleared out in some directions more than others by a precessing outflow. For example, the emission from the western wall of the outflow cavity shown in Figure 5 may extend to higher relative velocities than the eastern wall if the outflow has encountered less mass to the west, a direction along which gas may have been most recently cleared out by the precessing outflow. This scenario may also explain why the terminus of the outflow cavity appears to shift to the west with increasing relative velocity.

Figure 6 shows channel maps of the dense gas features near 4B, revealing the underlying structure of its outflow. Here, all features are found at increasingly large positional offsets from 4B with increasing relative velocity in a Hubble Law manner, except the feature east of 4B which moves in the opposite sense. Correspondingly, this latter feature may be emission from dense gas outflowing from 4B'. (Our mosaic does not cover area east of 4B' where other possible outflow features from 4B' could reside.)

The red features to the north and southeast and the blue features to the south and northwest seen in Figure 6 together suggest an X-shape, possibly indicative of outflow cavity walls similar to those surmised for the 4A blue lobe. In this case, the 4B dense gas outflow may consist of two lobes, one situated at a north-by-northwest P.A. (i.e., $\sim 345^\circ$) with an opening angle of $\sim 45^\circ$, and another at a south-by-southeast P.A. (i.e., $\sim 160^\circ$) with an opening angle of $\sim 30^\circ$. The peculiar appearance of both red and blue outflow emission on the same sides of 4B then may be due to the 4B outflow being inclined from the plane-of-sky at an angle less than, e.g., the $\sim 30^\circ$ opening angle of the narrower lobe. An alternative is that the brighter and dimmer pairs of symmetric red and blue dense gas outflow features are each independent outflows, with a projected difference in the orientation of their axes of ~ 30 – 45° , driven by unresolved objects within 4B. As with 4A, the H_2CO emission may still trace cavity walls in this case, but here they may be unresolved. A close companion to 4B is suggested by the sub-arcsecond resolution continuum data of Lay et al. and Looney et al. but this has not been yet confirmed.

4.2.2.2 Physical Properties of Outflows

Physical properties of the outflowing dense gas can be estimated from the H₂CO data, with some assumptions. To estimate the mass of outflowing gas, local thermodynamic equilibrium (LTE) was assumed and line emission was assumed to be optically thin, although these assumptions are likely not valid within dense gas outflows. To obtain de-projected relative gas velocities, both outflows were assumed to originate at the V_{LSR} of 4A or 4B (see §4.3.2) and are inclined 10° from the plane-of-sky due to the low spatial coincidence of their red and blue lobes. In addition, excitation temperature and H₂CO abundance values of $T_{ex} = 50$ K and $X(\text{H}_2\text{CO}) = 1.8 \times 10^{-7}$ or 4.3×10^{-7} were assumed for 4A or 4B respectively, as derived by B95 from wing emission.

Re-binning the original data cube to channels of width $\Delta V = 0.31$ km s⁻¹ (approximately the thermal broadening FWHM of H₂CO at 50 K, to obtain independent velocity channels l), the total gas mass of a given outflow feature k , M_k , can be estimated as

$$M_k = \frac{Z(T_{ex})}{g_j e^{-h\nu/kT_{ex}}} \frac{\mu m_H}{X(\text{H}_2\text{CO})} \sum_l^{\text{channels}} \int_{\Omega_{kl}} \frac{S_\nu^{kl} \Delta V}{A_{ji} h\nu} D^2 d\Omega, \quad (6)$$

where S_ν^{kl} and Ω_{kl} are the average flux density and deconvolved area of feature k in channel l obtained from two-dimensional Gaussian fits. (The projected distance to the nearest continuum object was also obtained from Gaussian fitting.) About 6 features were identified by eye within each of the 4A and 4B outflows, based on their $\geq 4\sigma$ peak intensities and persistence in several adjacent channels. In addition, A_{ji} is the Einstein A coefficient of the 3₁₂-2₁₁ line, ν is the line frequency, D is the assumed distance to IRAS 4, $Z(T_{ex})$ is the partition function of H₂CO at T_{ex} , and g_j is the degeneracy of the 3₁₂ level.

Masses (M_{out}) were obtained by summing Equation 6 over all features. Momenta (P_{out}) or kinetic energies (E_{out}) were obtained by summing the products of mass and relative de-projected velocity per channel, or the products of half the mass and the square of the relative de-projected velocity per channel respectively over all features. A characteristic timescale t was determined as the time for mass of a given feature at a given de-projected relative velocity to have travelled to a de-projected distance. (Given the extended nature of mass in each channel, t should not be mistaken for the actual time that all mass in the channel took to travel from the continuum source.) Dividing the momenta and kinetic energies per channel by these timescales per channel and summing over channels and features yielded total characteristic momentum fluxes (F_{H_2CO} , or forces) and mechanical luminosities (L_{mech} , or powers) of the outflows.

The total derived masses for the 4A and 4B dense gas outflows are $6.9 \times 10^{-4} M_{\odot}$ and $1.5 \times 10^{-4} M_{\odot}$ respectively. Table 4 lists these and the other physical properties derived for each dense gas outflow. The two brightest features associated with 4A or 4B contribute respectively 45% and 43% of M_{out} . Note that values for 4A listed in Table 4 include only the blue lobe of the 4A dense gas outflow, so total properties of the entire 4A dense gas outflow may be larger than those listed by a factor of ~ 2 , assuming the flow is symmetric, e.g., for a total L_{mech} of $0.25 L_{\odot} \text{ yr}^{-1}$.

Quantities in Table 4 for the 4A southern blue lobe alone exceed those of the all lobes of the 4B dense gas outflow by factors of 5–17. These differences may be significant if both outflows have similar low inclination angles, but this is a very uncertain assumption. For example, the mechanical luminosity, L_{mech} , of the 4A blue lobe would decrease by a factor of ~ 90 if the inclination of the flow were 45° instead of 10° , due to the intrinsically large dependence on $\tan i$. Differences between the 4A and 4B dense gas outflow characteristics could be expected from differences in the photon luminosities of the protostellar sources. Millimeter wavelength luminosities of 4A and 4B, obtained by integrating continuum flux densities in Table 2 and those at $\lambda = 450 \mu\text{m}$ and $\lambda = 850 \mu\text{m}$ by Sandell & Knee, are $0.24 L_{\odot}$ and $0.12 L_{\odot}$ respectively, only a factor of ~ 2 different. Other factors, therefore, may also be relevant.

Our values of M_{out} , P_{out} , and E_{out} for the 4A blue lobe are factors of ~ 60 – 80 less than values derived for the same lobe by Knee & Sandell, assuming their inclination angle (45°) and distance (220 pc). These differences are likely because the CO 3–2 data of Knee & Sandell (from the JCMT with a $14''$ FWHM beam) have greater sensitivity to large quantities of lower density gas (i.e., $n_{cr}[\text{CO 3–2}] \approx 10^4 \text{ cm}^{-3}$), suggesting dense gas (as seen by the H_2CO line) is relatively insignificant in terms of the total mass, momentum, and energy of the molecular outflow, comprising $< 2\%$ of these quantities. However, the momentum flux and mechanical luminosities we derive are only factors of ~ 10 less than those derived by Knee & Sandell for the 4A blue lobe, indicating the dense gas has greater significance in the total force and power of the 4A outflow.

4.3. N_2H^+ Observations

As discussed above, the N_2H^+ molecular ion can be relatively abundant in non-outflowing dense gas around protostellar objects, and the optical depth of its transitions can be low in all but the densest cases (e.g., L1544; see Williams et al. 1999). In addition, the N_2H^+ 1–0 transition has 7 hyperfine components from which the total brightness temperature (T_b^{tot}), the central line velocity (V_{LSR}), and the line width (ΔV) can be

estimated to good accuracy via simultaneous hyperfine structure fitting. These quantities can be used to estimate the mass of non-outflowing dense gas around 4A and 4B, and probe its rotational and incoherent motions.

Figure 7 shows the values of T_b^{tot} , V_{LSR} , and ΔV obtained from fitting the hyperfine structure of the N_2H^+ line around 4A and 4B, using the HFS routine of CLASS (see Caselli, Myers & Thaddeus 1995.) Values of ΔV shown were obtained by deconvolving the measured ΔV with the 0.16 km s^{-1} velocity resolution of the PdBI data. Typical errors from HFS fitting per pixel for T_b^{tot} , V_{LSR} , and ΔV were 0.94 K , 0.015 km s^{-1} , and 0.032 km s^{-1} respectively. The quantities shown in Figure 7 are restricted to those recovered from pixels containing data where the peak intensity of the brightest hyperfine component (i.e., N_2H^+ 123-012) was $\geq 5\times$ the rms of the respective spectral baseline. With this criterion, regions of dense gas surrounding each object are defined, similar in extent to those obtained by the lowest contour of Figure 1f from an integrated intensity criterion.

In Table 5, the mean, rms, minimum, and maximum values of T_b^{tot} , V_{LSR} , and ΔV in the non-outflowing dense gas surrounding 4A and 4B are summarized. To obtain these values, the fields shown in Figure 7 were re-binned into images with pixels $4''0 \times 3''5$ in size, about the area of the beam, so beam-averaged quantities at spatially independent locations could be examined. (Pixels not meeting the criterion for inclusion in Figure 7 were also not included in the re-binning.) Around 4B, the mean value of T_b^{tot} is $\sim 60\%$ larger than it is around 4A, but the mean values of V_{LSR} and ΔV are similar in both cases. However, the rms of V_{LSR} for the non-outflowing dense gas around 4A is $\sim 4\times$ larger than that for the same gas around 4B, a point discussed further in §4.3.2 below.

4.3.1. Column Densities and Masses

With quantities obtained from hyperfine structure fitting, the column density of N_2H^+ , $N(N_2H^+)$, in a given pixel around 4A and 4B can be estimated. Without unique estimates of T_{ex} and τ_{tot} , however, we assume $T_{ex} = 10 \text{ K} \gg hB/3k$, $T_{bg} = 2.73 \text{ K}$.¹⁰ In addition, we assume the line is optically thin (i.e., $T_b^{tot} \approx T_{ex}\tau_{tot}$), which is supported by the symmetric appearance of the line over the regions shown in Figure 7. Following similar estimates by Womack et al., but with these assumptions,

¹⁰ T_{bg} is much larger at the positions coincident with the peak continuum intensity, but since this is only significant for relatively few pixels, that difference is ignored here.

$$N(\text{N}_2\text{H}^+) \approx \frac{10^5}{1.06(J+1)} \frac{3h}{8\pi^3\mu^2} \frac{k(T_b^{\text{tot}})}{hB} \frac{e^{E_J/kT_{ex}}}{(1 - e^{-h\nu/kT_{ex}})} \Delta V, \quad (7)$$

where J is the upper rotational level (1), μ is the dipole moment of the N_2H^+ molecular ion (3.40 Debye; Green, Montgomery & Thaddeus 1974), B is the rotational constant of N_2H^+ (46.586702 GHz; Caselli et al.), E_J is the upper level energy ($= h\nu$ where $\nu=93.1734035$ GHz; Caselli et al.), and T_b^{tot} , and ΔV come from HFS fits. (Note that units for ΔV are km s^{-1} .)

From Equation 7, mean values of $N(\text{N}_2\text{H}^+)$ in the non-outflowing dense gas around 4A and 4B of $2.4 \times 10^{12} \text{ cm}^{-2}$ and $3.9 \times 10^{12} \text{ cm}^{-2}$ are found respectively. Table 5 also lists the rms, minimum, and maximum values for $N(\text{N}_2\text{H}^+)$ obtained for this gas around each protostellar object. (Decreasing T_{ex} to 5 K reduces the values of $N(\text{N}_2\text{H}^+)$ in Table 5 by only factors of $\sim 5\%$, but increasing T_{ex} to 20 K increases them by factors of $\sim 40\text{-}50\%$.) The mean column densities of non-outflowing dense gas around both objects are similar, although that of the gas around 4B is $\sim 60\%$ larger than that around 4A. These values are $2.5\text{-}5\times$ larger than the $N(\text{N}_2\text{H}^+)$ of $0.95 \times 10^{12} \text{ cm}^{-2}$ obtained from the mean N_2H^+ spectrum of IRAS 4 from single-dish data of M98, under the same assumptions. Maximum column densities listed in Table 5 are $5\text{-}8\times$ larger than this latter value. (The $N(\text{N}_2\text{H}^+)$ quantities listed in Table 5 are actually lower limits, given the assumption of $\tau_{\text{tot}} \rightarrow 0$, but the quantities should not vary much from those listed if $\tau_{\text{tot}} < 1$ as expected.)

With $N(\text{N}_2\text{H}^+)$, the masses of non-outflowing dense gas traced by N_2H^+ , M_{gas} , can be estimated by assuming the emission originates from gas local to 4A or 4B and not from gas distributed along the line-of-sight. With this assumption,

$$M_{\text{gas}} = \frac{\mu m_H}{X(\text{N}_2\text{H}^+)} D^2 \int_{\Omega_s} N(\text{N}_2\text{H}^+) d\Omega, \quad (8)$$

where μ , m_H , and D are the same as for Equation 6, but Ω_s is the solid angle subtended by the dense gas traced by N_2H^+ around each object, and $X(\text{N}_2\text{H}^+)$ is the fractional abundance of N_2H^+ .

For $X(\text{N}_2\text{H}^+)$, we assume for 4A and 4B the value of 6.0×10^{-11} derived by B95 at 4A by comparing the observed column density of N_2H^+ with that suggested for H_2 by continuum observations of dust. This value is relatively low compared to mean values found in other cloud cores; Womack et al. and Benson et al. found mean values of $X(\text{N}_2\text{H}^+)$ of 4×10^{-10} and 7×10^{-10} respectively from various samples (see also Ungerechts et al. 1997). However, the sample of Womack et al. contains several cases where $X(\text{N}_2\text{H}^+)$ is as low as or lower than 6.0×10^{-11} , e.g., ρ Oph and W49. Assuming a ‘‘canonical’’ CO abundance

of 1×10^{-4} , B95 also derived a value for $X(\text{N}_2\text{H}^+)$ of 6.0×10^{-10} , more similar to the mean values of other cloud cores, by comparing column densities of N_2H^+ with that of H_2 suggested by C^{18}O and C^{17}O data. B95 suggested this disparity could be reconciled if CO (and other molecules) in the non-outflowing gas of IRAS 4 were depleted relative to dust by factors of 10–20, but maintained abundances relative to each other that were similar to those seen elsewhere.

Using Equation 8 and the above assumptions, the M_{gas} of 4A and 4B are $0.73 M_\odot$ and $0.41 M_\odot$ respectively. As a comparison, recent SCUBA observations of continuum emission from dust around 4A and 4B by Sandell & Knee yield circumstellar mass estimates of $2.0\text{--}4.0 M_\odot$ and $0.65\text{--}1.3 M_\odot$, following their analysis but assuming a distance to NGC 1333 of 350 pc and a range of T_K of 20–40 K. (In their analysis, Sandell & Knee assumed $T_K = 25$ K and a 220 pc distance to derive masses.) The SCUBA-based masses are somewhat larger than ours, possibly due to their greater sensitivity to larger-scale emission from lower-density material.

Another comparison of mass is provided by virial masses of the non-outflowing dense gas surrounding 4A and 4B. These can be calculated from the respective mean values of ΔV and apparent sizes as

$$M_{vir} = 210 \left(\frac{R}{\text{pc}} \right) \left(\frac{\Delta V}{\text{km s}^{-1}} \right)^2 M_\odot, \quad (9)$$

for a uniform, self-gravitating sphere (e.g., see Larson 1981). Using the mean values of ΔV listed in Table 4, and the values of R of 0.022 pc for 4A and 0.0093 pc for 4B (obtained from the extents of the integrated emission shown in Figure 1f) in Equation 9, virial masses of $1.1 M_\odot$ and $0.48 M_\odot$ are found for the non-outflowing dense gas around 4A and 4B respectively, values quite similar to those determined above from the derived column densities. (Alternatively, values of $X(\text{N}_2\text{H}^+)$ of 4.0×10^{-11} and 5.1×10^{-11} , similar to that found by B95 for 4A, can be found for 4A and 4B respectively by inverting Equation 8 and assuming $M_{vir} = M_{gas}$.)

4.3.2. Rotation

Figures 7b and 7e show the distributions of V_{LSR} with position around 4A and 4B respectively obtained from hyperfine structure fitting. Systematic variations with position of the central velocity, V_{LSR} , of the symmetric profiles of an optically-thin line can suggest velocity gradients in the gas. If a gradient is found symmetrically about an average velocity

and position, it may be caused by rotational motions of the gas.

As listed in Table 5, the mean V_{LSR} values of the non-outflowing dense gas associated with 4A and 4B are 6.95 km s^{-1} and 6.98 km s^{-1} respectively, each within the mean fitting uncertainty of the other (0.032 km s^{-1}). If these mean velocities of this dense gas are representative of the radial velocities of the 4A and 4B objects themselves, the 4A and 4B objects are not moving relative to each other significantly along the line-of-sight, as might be expected if 4A and 4B were revolving about each other. (However, a V_{LSR} difference of 0.28 km s^{-1} is found between 4A and 4B from modeling their respective associated inverse P-Cygni profiles; see §4.2.1, Table 3.) The average V_{LSR} obtained from the non-outflowing dense gas around both objects is 6.96 km s^{-1} , which we take as the systemic velocity of IRAS 4.

Near 4A, the rms variation of V_{LSR} is more than half the mean ΔV , i.e., 0.36 km s^{-1} vs. 0.25 km s^{-1} , suggesting the variations of V_{LSR} around 4A are significant. Furthermore, the positional distribution of V_{LSR} in the non-outflowing dense gas about 4A shows systematic, symmetrical variations that may due to rotation. To first order, the southeastern half of this gas around 4A is blue-shifted (relative to the mean) by $\sim 0.25\text{-}0.5 \text{ km s}^{-1}$ and the northwestern half is red-shifted by $\sim 0.0\text{-}0.5 \text{ km s}^{-1}$, variations that could arise if this gas were rotating about 4A on an axis at a P.A. of $\sim 45^\circ$. (Such an axis would be colinear with the “cavity” containing 4A and 4A’.) Rotating dense gas, however, cannot account for all variations of V_{LSR} about 4A. For example, two pockets to the north-by-northwest and one to the south-by-southwest have relative velocities in directions opposite to those expected from rotation at their locations. Given that the south-by-southwest pocket is unusually red-shifted and that it lies in the same direction of the blue 4A outflow lobe (see §4.2.2), the pocket may be a local distortion of a rotational velocity field due to selective clearing of N_2H^+ at blue-shifted velocities by the outflow in that direction. A similar explanation may account for the unusually blue-shifted pockets in the same direction as the red outflow lobe. (The interpretation of velocity variations as caused by rotation is not unique, and the velocity distribution also could be due to bulk infall or outflow motions of gas on either side of 4A.)

Near 4B, the characteristics of V_{LSR} are much different from those seen around 4A. The rms variation of V_{LSR} is less than half the mean ΔV , i.e., 0.096 km s^{-1} vs. 0.25 km s^{-1} , and only $\sim 25\%$ that of the non-outflowing dense gas around 4A, suggesting the variations of V_{LSR} are not significant. In addition, no systematic variation of V_{LSR} is seen with position, and hence no suggestion of rotation (and infall or outflow), at least from the N_2H^+ 1–0 line. The difference in rotational properties between the non-outflowing dense gas surrounding 4A and 4B is striking in the context of binary formation. Since 4A is a known binary of $1''$

(or 350 AU) separation but 4B has not been confirmed to be a multiple, the relatively large rotation of the non-outflowing dense gas about 4A suggests binaries may form preferentially in cores of relatively high intrinsic angular momentum but single stars form preferentially in cores of relatively low intrinsic angular momentum. (However, 4B may be yet a binary system, albeit with a much smaller separation than that of 4A and 4A'; see §4.2.2).

4.3.3. *Turbulent Motions*

NGC 1333 is located in the western Perseus molecular cloud, a region where a large number of stars are forming in close proximity from gas that is fairly turbulent, judging from the observed line widths. For example, IRAS 4A and 4B have among the largest N_2H^+ 1–0 line widths, 1.32 km s^{-1} and 1.04 km s^{-1} respectively, of the 47 Class 0 or Class I objects within 400 pc sampled by M97. As the thermal FWHM of N_2H^+ is 0.247 km s^{-1} if $T_K = 40 \text{ K}$ (i.e., the maximum of the T_K range derived by B95 for the non-outflowing gas), the broad lines seen by M97 in IRAS 4 suggest the presence of substantial turbulent motions in the dense gas on scales of 0.05 pc (i.e., the 27" IRAM 30-m Telescope beam FWHM at 93.17 GHz at 350 pc.)

The PdBI data described here probes physical scales much smaller than those of single-dish observations, e.g., the synthesized beam FWHM is only $0.0055 \times 0.0064 \text{ pc}$ at 350 pc. Figures 7c and 7f show the distributions of the N_2H^+ 1–0 line width near 4A and 4B respectively, i.e., values of ΔV obtained from hyperfine structure fitting. Table 5 lists the beam-averaged mean, rms, maximum and minimum values of ΔV found for non-outflowing dense gas around 4A or 4B. From these data, a dramatic reduction in N_2H^+ line width is seen, relative to the single-dish data. For example, maximum beam-averaged values of ΔV around both objects are $<0.84 \text{ km s}^{-1}$, and the mean beam-averaged values of ΔV are both only $\sim 0.50 \text{ km s}^{-1}$, much less than seen in single-dish data.

At first glance, it is conceivable that the larger ΔV in single-dish observations could originate from the unresolved combination of intrinsically narrow lines with potentially wide variations of central line velocity in the dense gas (e.g., from rotation). However, the rms values of V_{LSR} and the mean values of ΔV are too small to support this possibility. Instead, the overall reduction of line width with scale in IRAS 4 may be a manifestation of the linewidth-size relation, as observed in many molecular clouds (e.g., see McKee 1999 and references therein), and the interferometer data is probing the smallest scales of this relation. At these scales, the nonthermal component of the line width is predicted to be comparable in magnitude to the thermal component, possibly due to dissipation of turbulence (Vazquez-Semadeni et al. 1999) or the cutoff of MHD wave propagation (Nakano

1998; Myers 1998) at small scales.

A similar but less dramatic reduction of line width with scale was noted for 8 “quiescent cores” in the Serpens NW cluster region by Williams & Myers, which is presumed to be at a similar distance to NGC 1333 (i.e., 310 pc; de Lara, Chavarría-K, & López-Molina 1991). In Serpens NW, the mean width ratio for lines observed between 10'' and 50'' resolution over all 8 cores was 0.59, whereas the mean width ratio for lines observed between $\sim 4''$ and 27'' over 4A and 4B is 0.43, using the observations of M98 and the mean values of ΔV in Table 5. Interestingly, the 8 cores found by Williams & Myers have typical sizes of ~ 5000 AU, line widths of ~ 0.5 km s $^{-1}$, and infall speeds of ~ 0.5 km s $^{-1}$, values all similar to those of the non-outflowing dense gas around 4A and 4B (assuming the infall speeds found in §4.2.1 from H $_2$ CO apply to the N $_2$ H $^+$ gas.)

Despite the overall relative reduction in line width with scale seen here, the high spatial resolution of these observations reveals significant variations in ΔV in the non-outflowing dense gas around both objects (see Figures 7c and 7f), and a common narrow width of ~ 0.5 km s $^{-1}$ cannot describe the line emission. Figure 8 shows histograms of the distributions of ΔV as fractions of the total number of beam-averaged pixels around 4A (54 pixels) or 4B (12 pixels) in 0.15 km s $^{-1}$ bins. Both have ranges of ΔV between 0.23 km s $^{-1}$ to 0.83 km s $^{-1}$, with substantial fractions (15-30%) near 0.25 km s $^{-1}$, the thermal line width at 40 K, indicating the presence of very non-turbulent gas around each object. (Minimum beam-averaged ΔV values of 0.21 km s $^{-1}$ near 4A and 0.16 km s $^{-1}$ near 4B are found, located north of 4A and 4B, or at the peripheries of the dense gas.) Of the remainder, the distribution for 4A has peaks at 0.38 km s $^{-1}$ and 0.68 km s $^{-1}$, but that of 4B has only a peak at 0.23 km s $^{-1}$. For 4A, lines of the first peak are located generally to the northwest and lines of the second peak are located generally to the southeast, although the populations are mixed. For 4B, the lines broaden systematically from north to south across its dense gas.

The condensations from which 4A and 4B formed may be plausibly assumed to have had nearly-uniform initial velocity dispersions, as is seen in many starless dense cores (see Goodman et al. 1998; Caselli et al. 2001). The star formation process from that time until the present likely increased the velocity dispersion by differing amounts throughout each condensation, due mainly to modest outflow-core interaction or heating from the protostars, but very likely did not decrease the dispersion anywhere. Every independent measurement of line width in the gas around each object then gives an upper limit on the initial velocity dispersion of the original condensation. The typical upper limit comes from the mean present-day line width, ~ 0.5 km s $^{-1}$ in both 4A and 4B, and the most constraining upper limit comes from the narrowest present-day line width, ~ 0.2 km s $^{-1}$ in the gas around both

4A and 4B. These new limits indicate that the initial level of turbulence in star-forming condensations may be very low, even in regions of clustered star formation. For example, if $T_K = 20$ K (the low end of T_K from B95) and $\Delta V(\text{observed}) = 0.225$ km s⁻¹ (the lowest ΔV bin in Figure 8), then $\Delta V(\text{thermal}) = 0.18$ km s⁻¹ for N₂H⁺ and $\Delta V(\text{nonthermal}) = 0.135$ km s⁻¹, as $\Delta V(\text{nonthermal}) = (\Delta V^2(\text{observed}) - \Delta V^2(\text{thermal}))^{0.5}$.

If the velocity dispersion has evolved from its initial state through the injection of energy, line widths arguably should be largest at positions closest to possible sources of energy, and there is indeed some evidence for this in the dense gas around both objects. For example, there appears to be some spatial correspondence between large values of ΔV and the blue-shifted outflow features (as traced by H₂CO) south of both 4A and 4B. However, the situation is not so clear cut and evidence to the contrary is also found. For example, the narrowest lines in the non-outflowing dense gas around 4A and 4B are found actually near the respective red outflow features north of each object. Moreover, large line widths are found across the southeastern half of the 4A dense gas, not just at positions near the blue outflow lobe. Given the factor of ~ 10 – 20 difference between the spectral width of the H₂CO wings and the width of the N₂H⁺ line even at positions of large ΔV , whatever coupling does exist between the dense outflowing gas and N₂H⁺ appears to be very inefficient.

The weak coupling between the fast outflow and the non-outflowing gas may be a consequence of their difference in speed, with greater coupling expected when the flow speed is more comparable to the velocity dispersion of its environment. On the other hand, possibly the N₂H⁺ is depleted more rapidly than it can be accelerated to speeds similar to the outflow. (The contrast of widths cannot be ascribed to the outflow gas being less dense than the non-outflowing gas, as both transitions probe gas at $n \approx 10^{5-6}$ cm⁻³.) Similar contrasts in line width have been found toward other very young objects, but the proximity of outflow gas to the non-outflowing gas is not so clearly defined in single-dish observations. For example, the survey of M97 contains several examples with outflow wings in H₂CO and CS, but not in N₂H⁺, on 0.02–0.05 pc scales, toward sources such as L483, S68N, or L1157 (and, of course, 4A and 4B). The PdBI data here show emission from both outflowing and non-outflowing gas around 4A and 4B can be spatially coincident on scales of only ~ 0.006 pc.

5. Summary and Conclusions

Millimeter interferometer observations are presented of NGC 1333 IRAS 4, a group of highly-embedded protostellar objects in the Perseus star-forming complex. Millimeter continuum data and line data allow the immediate dense gas and dust environments of

its protostellar objects to be characterized simultaneously at high spatial resolution. The major results found from these observations include:

1. Inverse P-Cygni profiles of H_2CO $3_{12}-2_{11}$ that show red-shifted absorption and blue-shifted emission have been detected toward 4A and 4B. Inverse P-Cygni profiles of CS $3-2$ and N_2H^+ $1-0$ also have been detected toward 4A. These profiles provide the least ambiguous evidence for infalling gas motions associated with low-mass young stellar objects. The depth of the absorption in the H_2CO line are equal to the $\lambda = 1.3$ mm continuum intensities of the protostars along the same lines-of-sight. Modeling the H_2CO profiles with a “two-layer” radiative transfer code, infall velocities toward 4A and 4B of 0.68 km s^{-1} and 0.47 km s^{-1} are estimated respectively. From these, masses of $0.53 M_\odot$ and $0.17 M_\odot$, and accretion rates, \dot{M}_{in} , of $1.1 \times 10^{-4} M_\odot \text{ yr}^{-1}$ and $3.7 \times 10^{-5} M_\odot \text{ yr}^{-1}$ for 4A and 4B are estimated respectively, given assumptions about r_{in} and n . Accretion timescales for both objects are similar, with $t_{acc} = \dot{M}/M$ of 4700 yr and 4600 yr for 4A and 4B respectively.

2. Outflowing gas from both 4A and 4B is detected from bright wing emission of H_2CO $3_{12}-2_{11}$ and CS $3-2$. The outflows from each source differ, in that only the southern blue lobe from the extended outflow from 4A is detected but 4-5 compact features from 4B are detected. For 4A, the velocity structure of the emission suggests the H_2CO is tracing outflow cavity walls. The orientation of the cavity walls suggests the outflow has precessed from orientations evident at larger scales, due possibly to the binarity of 4A. For 4B, the multipolar structure could be also from cavity walls of an outflow that is more compact than that from 4A. However, the complex structure may originate from several juxtaposed lobes from a multiple object.

3. Non-outflowing dense gas surrounding 4A and 4B individually is detected from N_2H^+ $1-0$ emission. With assumptions, we determine mean column densities of $2.4 \times 10^{12} \text{ cm}^{-2}$ and $3.9 \times 10^{12} \text{ cm}^{-2}$ respectively. Furthermore, masses of this gas are estimated to be $0.73 M_\odot$ and $0.41 M_\odot$ respectively, comparable to other estimates of circumstellar mass derived from submillimeter dust emission and the virial theorem. The variations of V_{LSR} around each object suggest the non-outflowing dense gas about 4A is rotating, but the data do not suggest similar motions about 4B.

4. The widths of the N_2H^+ $1-0$ line in the non-outflowing dense gas around both 4A and 4B are smaller by factors of 2–3 on average than those observed in single-dish data, due to the reduction of turbulent motions on smaller physical size scales. The data reveal a new, low upper bound to the initial velocity dispersion in the protostellar core from which IRAS 4 formed. For example, some regions around each object ($\sim 15-30\%$ of the projected surface areas of line emission) exhibit lines with very narrow widths, e.g., $\sim 0.2 \text{ km s}^{-1}$. Such narrow line widths are consistent with the incoherent motions of the gas

having a nonthermal component of a magnitude comparable to that of thermal broadening at expected gas temperatures, and may represent the initial state of the core gas prior to the formation of the protostars or their outflows. The lines show considerable variation of width, however, even on the small scales probed. Coupling between outflow and the non-outflowing dense gas, that could inject turbulent energy into any initially non-turbulent gas, appears highly inefficient, as line widths from H_2CO and N_2H^+ can differ by factors of 10–20 on scales of only 0.006 pc.

We acknowledge the generosity of many people who assisted with this study, in particular A. Dutrey, R. Neri, and the staff of the IRAM Plateau de Bure Observatory in France, M. Momose, N. Okumura, and the staff of the Nobeyama Radio Observatory in Japan, and M. Rupen, and the staff of the NRAO AOC in Socorro, New Mexico, U.S.A. We also thank an anonymous referee for many helpful comments, as well as Neal Evans, Lee Mundy, and Jeff Mangum for useful discussions. JD thanks the Smithsonian Astrophysical Observatory for a generous Fellowship, during which this study was begun. PCM acknowledges support from NASA Origins grant NAG5-6266. DM acknowledges support from FONDECYT 1990632.

A. High-Resolution Continuum Observations of NGC 1333 IRAS 4

Table 2 lists the flux densities, peak intensities, and deconvolved sizes of each source, derived from fitting single-component two-dimensional Gaussians to observations of each source individually at each wavelength with the AIPS task IMFIT. (Positions are also defined by these fits, e.g., those shown in Figure 1 are those of the peak continuum intensities at $\lambda = 1.3$ mm from Gaussian fitting.) Flux density uncertainties are comprised of those derived from the fits, an assumed 15% uncertainty in the absolute calibration at each wavelength, and an estimated 10% measurement uncertainty. Values in Table 2 for 4B' at $\lambda = 1.3$ mm are particularly uncertain due to its location at the mosaic edge (see Figure 1a), although the peak position obtained from the fit agrees quite well with those from other wavelengths.

Figure A1 shows the millimeter wavelength spectral energy distributions (SEDs) of each IRAS 4 object from our continuum data. In addition, Figure A1 shows data obtained at $\lambda = 800 \mu\text{m}$ by Lay et al. from the JCMT-CSO Interferometer, at $\lambda = 1.3$ cm and $\lambda = 3.6$ cm by Mundy et al. (1993) at the VLA, and at $\lambda = 3.6$ cm and $\lambda = 6.0$ cm by Rodriguez et al. (1999) at the VLA. At all wavelengths, 4A is brighter than 4B, which is in turn brighter than 4B'. The SEDs of Figure A1 are reasonably well fitted by straight lines

of similar slopes, i.e., $\alpha_1 = -2.7 \pm 0.05$ for 4A, -2.9 ± 0.14 for 4B, and -2.6 ± 0.23 for 4B', using linear least-squares fitting over the range $1.3 \text{ mm} < \lambda < 1.3 \text{ cm}$. (For 4A and 4B, only our data at $\lambda = 1.3 \text{ cm}$ was included for the fit, as they are similar (i.e., within errors) to those found by Mundy et al. at the same wavelength.) For 4B', the linear fit included the flux density at $\lambda = 1.3 \text{ mm}$, although this measurement is particularly uncertain, and excluded our upper limit at $\lambda = 1.3 \text{ cm}$.

The similar slopes reveal that continuum emission for the IRAS 4 objects at $\lambda < 1.3 \text{ cm}$ is dominated by thermal emission from dust grains surrounding each source. Given the deconvolved sizes of the emission, the warm dust being traced is likely situated within accretion disks or the inner radii of envelopes around each source. If the dust emission is optically thin (and we assume the same region is probed) at all wavelengths, the slope, α , can be used to estimate the indices of the mass opacity of dust, i.e., β . As $-\alpha = \beta + 2$ in the Rayleigh-Jeans limit, dust opacity indices of 0.7 ± 0.05 for 4A, 0.9 ± 0.14 for 4B, and 0.6 ± 0.25 for 4B' are found from our α_1 , each consistent with a common value of $\beta \approx 0.75$, and significantly less than the $\beta = 2$ value assumed typically for dust in the ISM. These values are similar to the $\beta \approx 1$ values inferred for dust around many other young stellar objects, a decrease in β possibly due to growth or composition changes of the dust (Beckwith & Sargent 1991).

The submillimeter wavelength data of Lay et al., not included in the linear fits shown in Figure A1, deviate from the derived fits because it was obtained at a resolution of $\sim 1''$, and much of the emission from dust in the inner radii of envelopes may have been resolved out in those data. The centimeter wavelength data of Rodriguez et al., also not included in the linear fits, deviate dramatically from the lines fit solely to the data at $\lambda \leq 1.3 \text{ cm}$, suggesting that free-free emission becomes increasingly dominant in the SEDs of these sources at long wavelengths. Extrapolating these data to shorter wavelengths, the contribution of this emission to the respective flux densities is small, i.e., $< 20\%$ at $\lambda = 1.3 \text{ cm}$ and $< 5\%$ at $\lambda = 6.9 \text{ mm}$ for both 4A or 4B.

Departures of individual flux densities at millimeter wavelengths from the linear fits are seen least in the fit to the 4B SED, whose reduced $\chi^2 = 1.6$, but are seen more for the fits to the 4A SED (reduced $\chi^2 = 7.9$) and 4B' SED (reduced $\chi^2 = 9.5$). These latter large values of reduced χ^2 may be due to underestimates of the absolute flux calibration uncertainties.

At specific wavelengths, the largest departures from the linear fits are the positive ones found at $\lambda = 3.2 \text{ mm}$ for all 3 objects. The object 3C 84 was also observed during all tracks as IRAS 4, but a similar positive departure of its flux density at $\lambda = 3.2$ from a linear fit is not seen. This consistency suggests the deviations in the IRAS 4 SEDs from their fits at

this wavelength may be real, and the slopes of the IRAS 4 SEDs at $\lambda \leq 3.2$ mm may be shallower than those found in earlier fits. Dust emission at $\lambda > 3.2$ mm may be declining at a steeper overall slope, possibly because the cooler, outer layers of the IRAS 4 envelopes are resolved out at our high resolutions, or have lower optical depths than the inner regions.

Slightly shallower slopes of the linear fits are found for the 4A and 4B SEDs if our VLA data are additionally excluded from the fits, i.e., $\alpha_2 = -2.6 \pm 0.29$ and -2.7 ± 0.30 respectively, but these do not differ significantly from slopes obtained with the VLA data included. One slope that does differ significantly is that of 4B', namely $\alpha_2 = -1.8 \pm 0.39$. The slopes of all three SEDs change only slightly if the NMA data are also excluded. Unlike for 4A and 4B, both α_1 and α_2 for 4B' are significantly more than the values of -3.8 or -3.9 derived by Choi (2001) from interferometer continuum data at $\lambda = 3.4$ mm and $\lambda = 2.7$ mm. Values of β derived from our slopes suggest so 4B' could have dust with significantly different opacity than 4A and 4B, possibly from a population of larger dust grains. Alternatively, the dust may be optically thick. Given the relative dimness of 4B' relative to 4A or 4B, more sensitive data than those shown here (especially at $\lambda = 1.3$ mm and $\lambda = 6.9$ mm) are needed to properly evaluate either possibility.

Table 1: Log of Observations

λ (mm)	ν (GHz)	Interferometer	Configuration	Observing Dates	Beam FWHM (")	Continuum rms (mJy beam ⁻¹)
1.3	225.7	IRAM PdBI	5C2-W09	21 Jul 1997	2.0×1.7	17.5
			4ant-special	19 Aug 1997		
			5D-N09	19 Sep 1997		
			4D2+N13	14 Nov 1997		
2.0	147.0	NMA	D	27 Dec 1997	3.2×2.3 ^a	14.0
			C	09 Mar 1998		
2.2	137.0	NMA	D	27 Dec 1997	3.4×2.6	10.5
			C	09 Mar 1998		
3.2	93.2	IRAM PdBI	5C2-W09	20 Jul 1997	2.9×2.6	4.5
			5C2-W09	21 Jul 1997		
			4ant-special	19 Aug 1997		
			5D-N09	19 Sep 1997		
			4D2+N13	14 Nov 1997		
6.9	43.3	VLA	D	25 Nov 1997	2.1×1.9	0.30
13.3	22.5	VLA	D	25 Nov 1997	3.8×3.1	0.28

^aCS 3–2 data tapered to a 6''5 × 4''4 FWHM beam for Figure 1e and analysis.

Table 2: Integrated Flux Densities, Peak Intensities and Deconvolved Sizes

Object	λ (mm)	S_{ν}^{total} (mJy)	I_{ν}^{peak} (mJy beam ⁻¹)	Deconvolved Size	
				Major \times Minor Axis (AU \times AU)	P.A. (degrees)
4A	1.3	3100 \pm 470	1200 \pm 16.	920 \times 720	132
	2.0	690 \pm 110	450 \pm 14.	770 \times 590	129
	2.2	580 \pm 90.	420 \pm 10.	740 \times 570	119
	3.2	320 \pm 49.	200 \pm 4.4	790 \times 650	177
	6.9	26. \pm 4.0	16. \pm 0.29	580 \times 490	138
	13.3	4.7 \pm 0.95	3.1 \pm 0.27	1100 \times 630	125
4B	1.3	1100 \pm 170	590 \pm 17.	600 \times 560	151
	2.0	320 \pm 56.	250 \pm 14.	630 \times 390	119
	2.2	240 \pm 41.	210 \pm 11.	440 \times 300	151
	3.2	93. \pm 16.	90. \pm 4.5	<570 \times <570	...
	6.9	7.8 \pm 1.3	5.8 \pm 0.29	630 \times 110	128
	13.3	1.2 \pm 0.56	1.0 \pm 0.28	<1400 \times <1400	...
4B'	1.3	230 \pm 47.	200 \pm 18.	<640 \times <640	...
	2.0	79. \pm 29.	70. \pm 14.	<840 \times <840	...
	2.2	82. \pm 21.	89. \pm 10.	<780 \times <780	...
	3.2	45. \pm 11.	41. \pm 4.5	<690 \times <690	...
	6.9	2.2 \pm 0.65	1.9 \pm 0.30	<840 \times <840	...
	13.3	<0.84	<0.84

Table 3: “Two-layer” Model Parameters for Inverse P-Cygni Profiles^a

Object	τ_o	Φ	J_c (K)	J_f (K)	J_r (K)	V_{LSR} (km s ⁻¹)	σ (km s ⁻¹)	V_{in} (km s ⁻¹)
4A	2.0	0.3	45	3	19	6.85	0.34	0.68
4B	1.6	0.3	30	3	20	7.13	0.51	0.47

^asee Figure 4 for model profiles.

Table 4: Physical Quantities of Mass Flows in NGC 1333 IRAS 4

Derived Quantity	Abbreviation	(units)	IRAS 4A ^a	IRAS 4B ^b
<i>Infall^c:</i>				
Mass Accretion Rate	\dot{M}_{in}	$M_{\odot} \text{ yr}^{-1}$	1.1×10^{-4}	3.7×10^{-5}
<i>Outflow^d:</i>				
Mass	M_{out}	M_{\odot}	6.9×10^{-4}	1.5×10^{-4}
Momentum	P_{out}	$M_{\odot} \text{ km s}^{-1}$	1.6×10^{-2}	1.6×10^{-3}
Kinetic Energy	E_{out}	erg	4.9×10^{42}	3.2×10^{41}
Momentum Flux	F_{H_2CO}	$M_{\odot} \text{ km s}^{-1} \text{ yr}^{-1}$	4.2×10^{-5}	3.2×10^{-6}
Mechanical Luminosity	L_{mech}	L_{\odot}	1.3×10^{-1}	7.4×10^{-3}

^asouthern blue lobe only.

^bincludes contribution from eastern blue lobe, some of which may originate from 4A'; see text.

^cderived from very uncertain r_{in} ; see text.

^dfor dense gas in outflow only; assumes outflow inclination angle of 10° for both 4A and 4B.

Table 5: N_2H^+ Line Properties Derived from Hyperfine Structure Fits

Value	Unit	4A				4B			
		mean	rms	min	max	mean	rms	min	max
T_B^{tot}	K	7.8	2.1	3.6	13.	12.	4.4	4.8	21.
V_{LSR}	km s ⁻¹	6.95	0.359	6.48	8.2	6.98	0.0928	6.75	7.38
ΔV	km s ⁻¹	0.49	0.17	0.21	0.83	0.50	0.20	0.16	0.81
$N(N_2H^+)$	10 ¹² cm ⁻²	2.4	1.2	0.54	5.1	3.9	1.9	0.77	7.7

REFERENCES

- Adelson, L. M., & Leung, C. M. 1988, MNRAS, 235, 349
- Akeson, R. L., Carlstrom, J. E., Phillips, J. A., & Woody, D. P. 1996, ApJ, 456, L45
- André, P., Ward-Thompson, D., & Barsony, M. 1993, ApJ, 406, 122
- Arons, J., & Max, C. E. 1975, ApJ, 196, L77
- Bachiller, R. 1996, ARA&A, 34, 111
- Bachiller, R., & Pérez-Gutiérrez, M. 1997, ApJ, 487, L93 (BP)
- Beckwith, S. V. W., & Sargent, A. I. 1991, ApJ, 381, 250
- Benson, P. J., Caselli, P., & Myers, P. C. 1998, ApJ, 506, 743
- Bergin, E. A., Neufeld, D. A., & Melnick, G. J. 1998, ApJ, 499, 777
- Bergin, E. A., & Langer, W. D. 1997, ApJ, 486, 316
- Blake, G. A., Sandell, G., van Dishoeck, E. F., Groesbeck, T. D., Mundy, L. G., & Aspin, C. 1995, ApJ, 441, 689 (B95)
- Bontemps, S., André, P., Terebey, S., & Cabrit, S. 1996, A&A, 311, 858
- Cabrit, S., & Bertout, C. 1986, ApJ, 307, 313
- Caselli, P., Benson, P. J., Myers, P. C., & Tafalla, M. 2001, in preparation
- Caselli, P., Myers, P. C., & Thaddeus, P. 1995, ApJ, 455, L77
- Černis, K. 1990, ApSS, 166, 315
- Choi, M. 2001, ApJ, in press
- Choi, M., Panis, J.-F., & Evans, N. J. II 1999, ApJS, 122, 519
- Crutcher, R. 1999, ApJ, 520, 706
- de Lara, E., Chavarria-K, C., & Lopez-Molina, G. 1991, A&A, 243, 139
- Di Francesco, J., Evans, N. J. II, Harvey, P. M., Mundy, L. G., Guilloteau, S., & Chandler, C. J. 1997, ApJ, 482, 433
- Di Francesco, J., Myers, P.C., & Wilner, D. J. 2002, in preparation
- Evans, N. J. II 1999, ARA&A, 37, 311
- Goodman, A. A., Barranco, J. A., Wilner, D. J., & Heyer, M. H. 1998, ApJ, 504, 223
- Green, S. 1991, ApJS, 76, 979
- Green, S., Montgomery, J. A. Jr., & Thaddeus, P. 1974, ApJ, 193, L89

- Gregersen, E., Evans, N. J. II, Zhou, S., & Choi, M. 1997, *ApJ*, 484, 256
- Herbig, G. H., & Jones, B. F. 1983, *AJ*, 88, 1040
- Ho, P. T. P., & Young, L. M. 1996, *ApJ*, 472, 742
- Jennings, R. E., Cameron, D. H. M., Cudlip, W., & Hirst, C. J. 1987, *MNRAS*, 226, 461
- Keto, E., Ho, P. T. P., Haschick, A. D., 1987, *ApJ*, 318, 712
- Keto, E., Ho, P. T. P., Haschick, A. D., 1988, *ApJ*, 324, 920
- Knee, L. B. G., & Sandell, G. 2000, *A&A*, 361, 671
- Lada, E. A., Strom, K. M., & Myers, P. C. 1993, in *Protostars & Planets III*, ed. E. H. Levy, J. I. Lunine, & M. S. Matthews (Tucson: Univ. Arizona Press), 245
- Larson, R. B. 1981, *MNRAS*, 194, 809
- Lay, O. P., Carlstrom, J. E., & Hills, R. E. 1995, *ApJ*, 452, L73
- Lee, C. W., Myers, P. C., & Tafalla, M. 2001, *ApJS*, in press
- Lefloch, B., Castets, A., Cernicharo, J., Langer, W. D., & Zylka, R. 1998, *A&A*, 334, 269
- Leung, C. M., & Brown, R. L. 1977, *ApJ*, 216, L73
- Looney, L. W., Mundy, L. G., & Welch, W. J. 2000, *ApJ*, 529, 477
- Mardones, D., Myers, P. C., Tafalla, M., Wilner, D. J., Bachiller, R., & Garay, G. 1997 (M97), 465, 133
- Mardones, D. 1998, PhD Thesis, Harvard University (M98)
- Mardones, D., Myers, P. C., Tafalla, M., Bachiller, R., Wilner, D. J., & Garay, G. 2001, *ApJ*, submitted
- Mathieu, R. D. 1994, *ARA&A*, 32, 465
- McKee, C. F. 1999, in *The Origin of Stars and Planetary Systems*, ed. C. J. Lada, & N. D. Kylafis (Dordrecht: Kluwer), 29
- Mundy, L. G., McMullin, J. P., Grossman, A. W., & Sandell, G. 1993, *Icarus*, 106, 11
- Myers, P. C. 1998, *ApJ*, 496, L109
- Myers, P. C., Mardones, D., Tafalla, M., Williams, J. P., & Wilner, D. J. 1996, *ApJ*, 465, L133
- Nakano, T. 1998, *ApJ*, 494, 587
- Ohashi, N., Hayashi, M., Ho, P. T. P., Momose, M., Tamura, M., Hirano, N., & Sargent, A. I. 1997, *ApJ*, 488, 317

- Plambeck, R. L. & Engargiola, G. 1999, in ASP Conf. Ser. 217, Imaging at Radio Through Submillimeter Wavelengths, ed. J. G. Mangum, & S. J. E. Radford, (San Francisco: ASP), 354
- Rodriguez, L. F., Anglada, G., & Curiel, S. 1999, ApJS, 125, 427
- Sandell, G., & Knee, L. B. G. 2000, ApJ, 546, L49
- Sandell, G., Aspin, C., Duncan, W. D., Russell, A. P. G., & Robson, E. I. 1991, ApJ, 376, L17
- Smith, K. W., Bonnell, I. A., Emerson, J. P., & Jenness, T. 2000, MNRAS, 319, 991
- Ungerechts, H., Bergin, E. A., Goldsmith, P. F., Irvine, W. M., Schlorb, F. P., & Snell, R. L. 1997, ApJ, 482, 245
- Vázquez-Semadeni, E., Ostriker, E. C., Passot, T., Gammie, C. F., & Stone, J. M. 2000, in Protostars and Planets IV, ed. V. Mannings, A. P. Boss, S. S. Russell (Tucson, Univ. Arizona Press), 3
- Webster, Z. T., & Welch, W. J. 2000, private communication
- Welch, W. J., Dreher, J. W., Jackson, J. M., Terebey, S., & Vogel, S. N. 1987, Science, 238, 1550
- Williams, J. P., & Myers, P. C. 2000, ApJ, 537, 891
- Williams, J. P., Myers, P. C., Wilner, D. J., & Di Francesco, J. 1999, ApJ, 513, L61
- Womack, M., Ziurys, L. M., & Wyckoff, S. 1992, ApJ, 387, 417
- Zhang, Q., & Ho, P. T. P. 1997, ApJ, 488, 241
- Zhang, Q., Ho, P. T. P., & Ohashi, N. 1998, ApJ, 494, 636
- Zhou, S., Evans, N. J. II, Koempe, C., & Walmsley, C. M. 1993, ApJ, 404, 232

Fig. 1.— Millimeter continuum and line interferometer maps of NGC 1333 IRAS 4. Positions of continuum sources 4A, 4B, and 4B' at $\lambda = 1.3$ mm are denoted by *large black stars* while the position of continuum source 4A' from Looney et al. (2000) is denoted by a *smaller black star*. The *black ellipses* placed in the bottom left of each panel represent the FWHMs of the respective synthesized beams. Outer dashed contours represent the masking cutoffs at a specific gain level of the mosaics: 20% for the IRAM PdBI, or 50% for the NRO NMA data. *a)* $\lambda = 1.3$ mm continuum emission. *Plain contours* start at $52.5 \text{ mJy beam}^{-1}$ (3σ), increasing in steps of 2σ to $297.5 \text{ mJy beam}^{-1}$; the *dashed contour* denotes $-52.5 \text{ mJy beam}^{-1}$. *b)* $\lambda = 2.0$ mm continuum emission. *Plain contours* start at $42.0 \text{ mJy beam}^{-1}$ (3σ), increasing in steps of 2σ to $126.0 \text{ mJy beam}^{-1}$; the *dashed contour* denotes $-42.0 \text{ mJy beam}^{-1}$. *c)* $\lambda = 3.2$ mm continuum emission. *Plain contours* start at $13.5 \text{ mJy beam}^{-1}$ (3σ), increasing in steps of 2σ to $49.5 \text{ mJy beam}^{-1}$; dashed contour denotes $-13.5 \text{ mJy beam}^{-1}$. The *arrows* to the northeast and southwest of 4A+4A' denote the directions of the large-scale CO outflow detected by Blake et al. (1995) *d)* The integrated intensity of $\text{H}_2\text{CO } 3_{12}-2_{11}$ emission (“zerth-moment”; see text). The *bold contour* shows the half-maximum isophote (57 K km s^{-1}), while *plain contours* step up and down in increments of 1.5σ (10.5 K km s^{-1}) from this level. *e)* The integrated intensity of CS 3–2 emission. The *bold contour* shows the half-maximum isophote (11.1 K km s^{-1}), while *plain contours* step up and down in increments of 1.5σ (4.5 K km s^{-1}) from this level. *f)* The integrated intensity of $\text{N}_2\text{H}^+ 1-0$ emission (over all 7 hyperfine components). The *bold contour* shows the half-maximum isophote (7.6 K km s^{-1}), while *plain contours* step up and down in increments of 1.5σ (1.2 K km s^{-1}) from this level.

Fig. 2.— Grids of $\text{H}_2\text{CO } 3_{12}-2_{11}$ spectra at selected positions at and around 4A and 4B. In both grids, panels are spaced by $2''$ in R.A. or Dec., ~ 1 FWHM of the beam at 225.7 GHz, the $\text{H}_2\text{CO } 3_{12}-2_{11}$ rest frequency, so adjacent panels in the H_2CO grid are independent. The dashed line represents the determined V_{LSR} of the IRAS 4 system of 6.96 km s^{-1} . *a) top grid:* Panels centered at the 4A position at $\lambda = 1.3$ mm (R.A. (2000) = 03:29:10.5, Dec. (2000) = +31:13:31.4). *b) bottom grid:* Panels centered at the 4B position of 4B at $\lambda = 1.3$ mm (R.A. (2000) = 03:29:12.0, Dec. (2000) = +31:13:08.2).

Fig. 3.— Grids of $\text{N}_2\text{H}^+ 1-0$ spectra at the same positions at and around 4A and 4B defined for Figure 2. Due to the larger beam at 93.17 GHz, the $\text{N}_2\text{H}^+ 1-0$ rest frequency, the adjacent panels are not independent, as in Figure 2. In addition, the velocity range in each panel here is wider relative that of to Figure 2, although panels in both Figures are centered at the same velocity.

Fig. 4.— $\text{H}_2\text{CO } 3_{12}-2_{11}$ spectra from the IRAM PdBI toward the positions of peak continuum intensity near 4A (*panel a*) and 4B (*panel b*). The *dotted line* denotes the average systemic

V_{LSR} of $+6.96 \text{ km s}^{-1}$. In each panel, a *dashed line* shows a spectrum resulting from a simple two-layer model of infall toward each object. Respective model parameters are listed in Table 3.

Fig. 5.— Channel maps of $\text{H}_2\text{CO } 3_{12}-2_{11}$ emission revealing the underlying structure of the southern blue lobe of the 4A dense gas outflow. Each channel is the mean of 3 channels of the original data cube, and has a channel width of 0.3113 km s^{-1} . The velocity of a given panel is shown at the upper left in km s^{-1} ; only a fraction of channels blueward of the systemic velocity are shown. Continuum positions of 4A and 4A' are denoted by *large stars* and *small stars* respectively. *Solid contours* begin at 3.5 K and increase in steps of 3.5 K, and *dashed contours* begin at -3.5 K and decrease in steps of -3.5 K . The *grey scale* ranges from -3.5 K to 28.2 K .

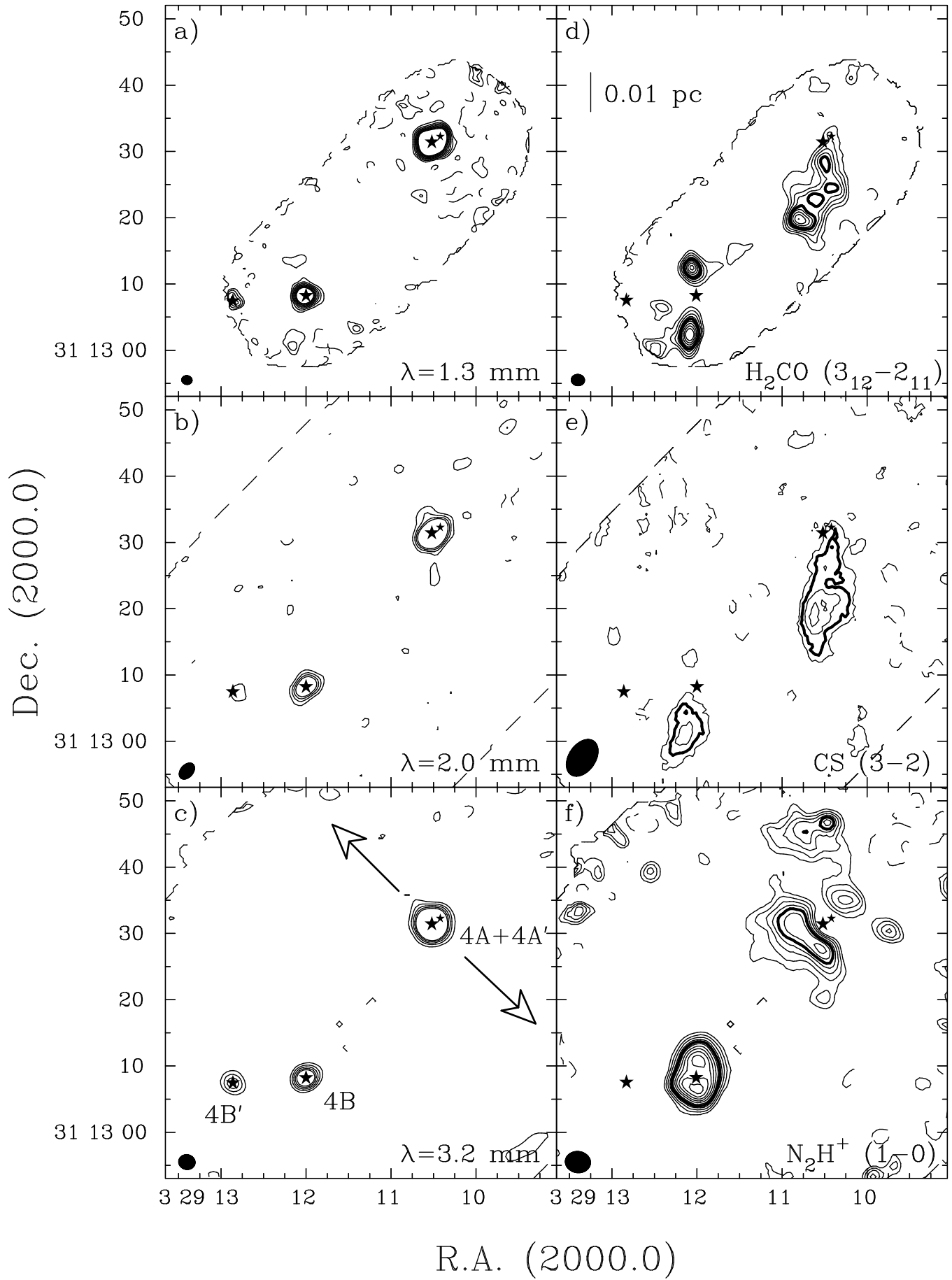
Fig. 6.— Channel maps of $\text{H}_2\text{CO } 3_{12}-2_{11}$ emission depicting the red and blue lobes of the 4B dense gas outflow. Channel width, contours, grey scales, and symbols are the same as described for Figure 5, except *stars* denote the continuum locations of 4B (near center) and 4B' (to the left). In addition, an equal number of channels redward and blueward of the systemic velocity of 4B are shown.

Fig. 7.— The spatial distribution of T_B^{tot} , V_{LSR} and ΔV of the $\text{N}_2\text{H}^+ 1-0$ line around IRAS 4A and 4B, obtained by fitting the 7 hyperfine components of the line simultaneously with the HFS fitting routine of CLASS. Only positions where the peak intensity of brightest hyperfine component was $\geq 5 \times$ the spectral baseline rms are shown, and data at other positions have been blanked. The positions of continuum objects 4A, 4A', and 4B, are represented by *stars*, and are the same positions as denoted in Figure 1. a) Distribution of T_B^{tot} around 4A, where the color scale is defined from 0 K to 40 K, and contours begin at 2.5 K and continue in increments of 2.5 K to 40.0 K. b) Distribution of V_{LSR} around 4A, where the color scale is defined from 6.0 km s^{-1} to 8.0 km s^{-1} , and contours begin at 6.2 km s^{-1} and increase in increments of 0.2 km s^{-1} to 7.8 km s^{-1} . c) Distribution of ΔV around 4A, where the color scale is defined from 0.1 km s^{-1} to 1.5 km s^{-1} , and contours begin at 0.2 km s^{-1} and increase in increments of 0.2 km s^{-1} to 1.4 km s^{-1} . d) Distribution of T_B^{tot} around 4B, with the same color scale and contour levels defined for panel a). e) Distribution of V_{LSR} around 4B, with the same color scale and contour levels defined for panel b). f) Distribution of ΔV around 4B, with the same color scale and contour levels defined for panel c).

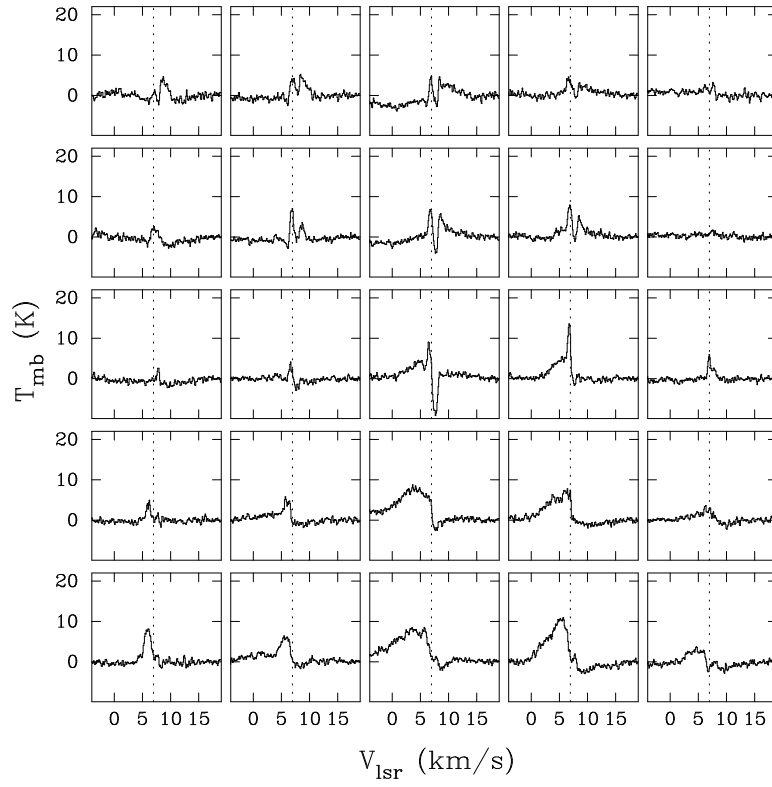
Fig. 8.— Distribution of ΔV from $\text{N}_2\text{H}^+ 1-0$ emission around 4A (*panel a*) and 4B (*panel b*) in 0.15 km s^{-1} wide bins as fractions of the total number of non-blanked pixels, i.e., 54 pixels for 4A and 12 pixels for 4B. (The criterion for blanking is the same as for Figure 7.) Values of ΔV are obtained by deconvolving the measured values by the 0.16 km s^{-1} velocity

resolution of the PdBI correlator. The *dashed line* indicates the FWHM expected from the N_2H^+ 1–0 line from thermal broadening only at $T_K = 40$ K, the maximum T_K estimated for the non-outflowing gas around 4A by B95. The *dot-dashed line* indicates the mean ΔV measured from spectra around each protostellar object.

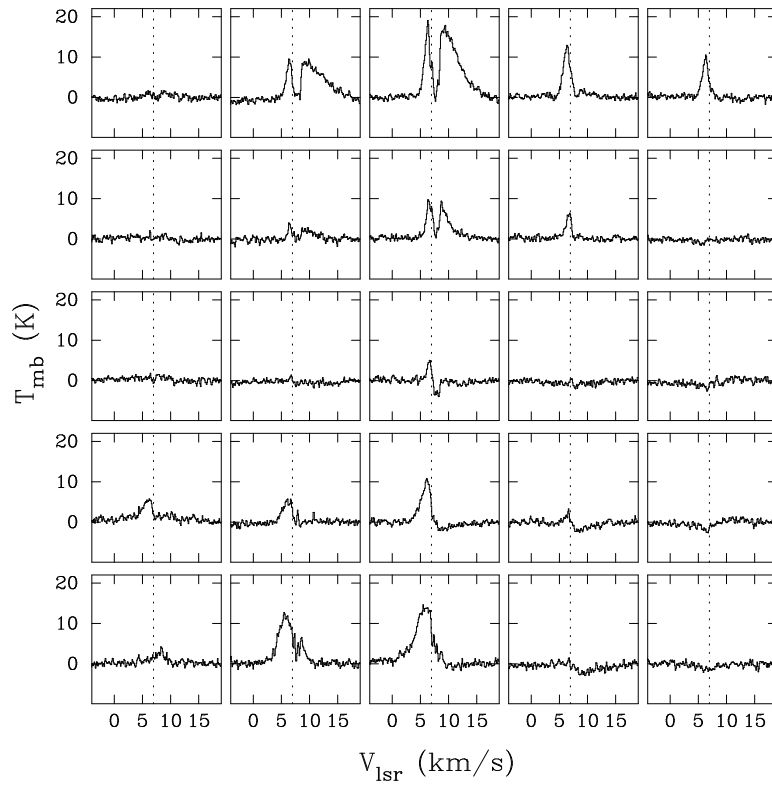
Fig. A1.— Spectral energy distributions of 4A, 4B, and 4B' objects from interferometer continuum observations between $\lambda = 800 \mu\text{m}$ to $\lambda = 6$ cm. *Filled squares, filled triangles, or filled stars* show data obtained respectively from the IRAM PdBI, the NRO NMA, or the NRAO VLA for this paper. The *open circles* show data at $\lambda = 800 \mu\text{m}$ from the JCMT-CSO Interferometer by Lay, Carlstrom, & Hills (1995) for 4A and 4B. *Open squares* show data at $\lambda = 1.3$ cm and $\lambda = 3.6$ cm from Mundy et al. (1993) and *open diamonds* show data at $\lambda = 3.6$ cm and $\lambda = 6.0$ cm by Rodriguez et al. (1999) for 4A and 4B all from the Very Large Array. *Downward-pointing arrows* indicate 3σ upper limits. *Error bars* are 1σ (see text and Table 2). *Solid lines* indicate lines of slope α_1 from resulting from linear least-squares fits to our flux densities of each object at $1.3 \text{ mm} < \lambda < 1.3 \text{ cm}$. *Dashed lines* indicate lines of slope α_2 resulting from similar fitting but using only our data at $1.3 \text{ mm} < \lambda < 3.2 \text{ mm}$.



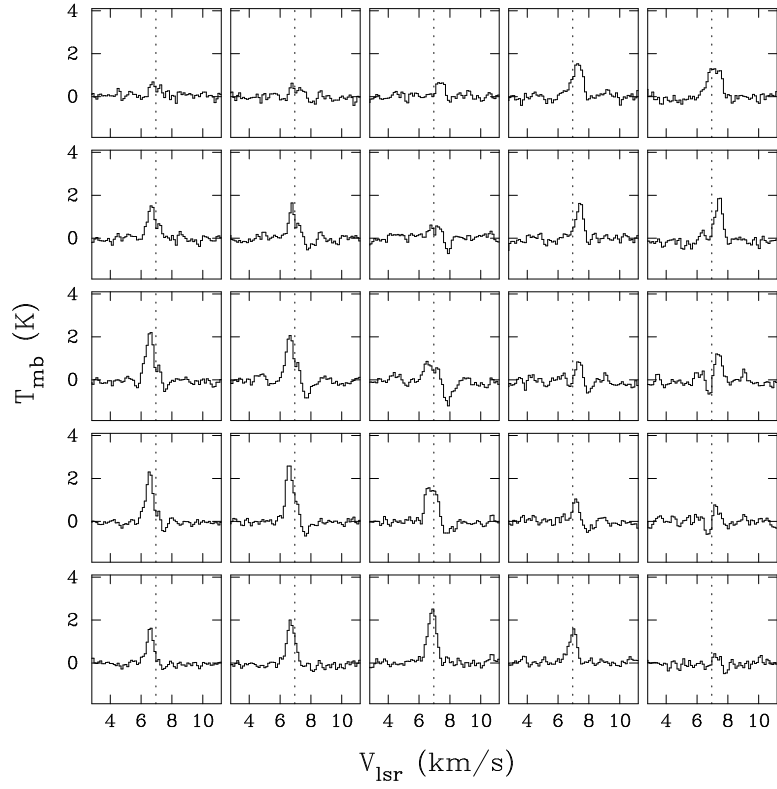
a) 4A: $\text{H}_2\text{CO } 3_{12}-2_{11}$



b) 4B: $\text{H}_2\text{CO } 3_{12}-2_{11}$



a) 4A: N_2H^+ 101-012



b) 4B: N_2H^+ 101-012

